



# Effects of strain rate on mechanical properties and deformation behavior of an austenitic Fe-25Mn-3Al-3Si TWIP-TRIP steel



J.T. Benzing<sup>a,\*</sup>, W.A. Poling<sup>b</sup>, D.T. Pierce<sup>b,c</sup>, J. Bentley<sup>d</sup>, K.O. Findley<sup>b</sup>, D. Raabe<sup>e</sup>, J.E. Wittig<sup>a</sup>

<sup>a</sup> Interdisciplinary Materials Science, Vanderbilt University, Nashville, TN 37235-1683, USA

<sup>b</sup> Advanced Steel Processing and Products Research Center, Colorado School of Mines, Golden, CO 80401, USA

<sup>c</sup> Materials Science and Technology Division, Oak Ridge National Laboratory, 1 Bethel Valley Rd, Oak Ridge, TN 37831, USA

<sup>d</sup> Microscopy and Microanalytical Sciences, P O Box 7103, Oak Ridge, TN 37831-7103, USA

<sup>e</sup> Max-Planck-Institut für Eisenforschung, Max-Planck-Str. 1, 40237 Düsseldorf, Germany

## ARTICLE INFO

### Keywords:

High-Mn [Fe-25Mn-3Al-3Si] steel  
Strain rate sensitivity  
Adiabatic heating  
Stacking fault energy (SFE)  
Twinning and transformation-induced plasticity (TWIP-TRIP)

## ABSTRACT

The effects of quasi-static and low-dynamic strain rate ( $\dot{\epsilon} = 10^{-4}$  /s to  $\dot{\epsilon} = 10^2$  /s) on tensile properties and deformation mechanisms were studied in a Fe-25Mn-3Al-3Si (wt%) twinning and transformation-induced plasticity [TWIP-TRIP] steel. The fully austenitic microstructure deforms primarily by dislocation glide but due to the room temperature stacking fault energy [SFE] of  $21 \pm 3$  mJ/m<sup>2</sup> for this alloy, secondary deformation mechanisms such as mechanical twinning (TWIP) and epsilon martensite formation (TRIP) also play an important role in the deformation behavior. The mechanical twins and epsilon-martensite platelets act as planar obstacles to subsequent dislocation motion on non-coplanar glide planes and reduce the dislocation mean free path. A high-speed thermal camera was used to measure the increase in specimen temperature as a function of strain, which enabled the use of a thermodynamic model to predict the increase in SFE. The influence of strain rate and strain on microstructural parameters such as the thickness and spacing of mechanical twins and epsilon-martensite laths was quantified using dark field transmission electron microscopy, electron channeling contrast imaging, and electron backscattered diffraction. The effect of sheet thickness on mechanical properties was also investigated. Increasing the tensile specimen thickness increased the product of ultimate tensile strength and total elongation, but had no significant effect on uniform elongation or yield strength. The yield strength exhibited a significant increase with increasing strain rate, indicating that dislocation glide becomes more difficult with increasing strain rate due to thermally-activated short-range barriers. A modest increase in ultimate tensile strength and minimal decrease in uniform elongation were noted at higher strain rates, suggesting adiabatic heating, slight changes in strain-hardening rate and observed strain localizations as root causes, rather than a significant change in the underlying TWIP-TRIP mechanisms at low values of strain.

## 1. Introduction

Within the past decade, advanced high strength steels (AHSS) have been incorporated into automotive vehicles to reduce their weight and improve the strength of structural components [1–3]. More stringent fuel economy standards and crash tests continue to drive the implementation and evolution of AHSS. High-manganese twinning-induced and transformation-induced plasticity (TWIP/TRIP) steels exhibit promising properties for automotive applications due to their exceptional combination of strength and ductility. The product of ultimate tensile strength (UTS) and total elongation (TE) typically ranges between 42,000 and 68,000 MPa% [4–6], which is superior to many other AHSS grades. The superior energy absorption capability of these steels

could also play a critical role in improving crash performance for future vehicle designs.

Typically, high-Mn (15–30 wt%) TWIP and/or TRIP steels are composed of metastable or stable austenite and are alloyed with Al, Si, Cr, C and N [5–12]. The deformation mechanisms and tensile properties of TWIP and/or TRIP steels can exhibit a strong dependence on temperature and/or stacking-fault energy (SFE) [4,7]. These steels deform by a combination of dislocation glide and secondary deformation mechanisms such as mechanical twinning and/or  $\epsilon_{\text{hcp}}$ -martensite formation [13,4]. Austenitic high-Mn steels with relatively high SFE (approximately 50 mJ/m<sup>2</sup> and greater) deform primarily by dislocation glide. As the SFE decreases from  $\sim 50$  to  $\sim 20$  mJ/m<sup>2</sup>, mechanical twinning becomes increasingly favorable and the steel deforms by both

\* Corresponding author.

E-mail address: [jake.t.benzing@vanderbilt.edu](mailto:jake.t.benzing@vanderbilt.edu) (J.T. Benzing).

dislocation glide and mechanical twinning. With decreasing SFE below  $\sim 20 \text{ mJ/m}^2$ , these steels typically deform by a combination of dislocation glide and a martensitic phase transformation, where the austenite phase transforms to hexagonal epsilon martensite [4,7,10,14–18]. The mechanisms by which mechanical twins and epsilon martensite form are closely related to the glide of  $a/6 < 112 >$  partial dislocations, which both trail and lead a stacking fault on  $\{111\}$  glide planes [8,19–23]. The martensite platelets and mechanical twins act as planar obstacles, reduce the mean free path of non-coplanar dislocation glide and produce back stresses, resulting in a high strain-hardening rate, delayed necking, and large uniform elongations [5–10,23–26].

A fundamental understanding of the deformation mechanisms of TWIP-TRIP steels at high strain rates will be beneficial for implementing these steels into automotive vehicles and designing future TWIP-TRIP steel grades, particularly as it relates to the response of TWIP-TRIP steels to high strain rates experienced during crashes and advanced forming processes [27]. Under crash conditions, steel components are subjected to a wide range of strain rates, most of which can be simulated with tensile tests in the strain rate range of  $\dot{\epsilon} = 10^{-2} \text{ /s}$  to  $\dot{\epsilon} = 10^3 \text{ /s}$  [28]. Implementation of complex geometries and varying thicknesses of automotive body parts requires a deeper understanding of TWIP-TRIP steel behavior at high strain rates, since many studies on sheet steels have shown an influence of specimen thickness on mechanical properties [29–33]. Interrupted tests are essential for gaining an in-depth understanding of how next-generation steels behave at high strain rates. Interrupted high-rate tests with electromagnetic forming have been reported as far back as 1982 and allow for characterization of the microstructure at appropriate levels of strain [34]. Choi et al. [35] measured the volume fraction of retained austenite in two different TRIP sheet steels as a function of strain at rates up to  $\dot{\epsilon} = 6 \times 10^2 \text{ /s}$  with the use of an interruption device during high strain rate tensile testing. The methodology to interrupt high strain rate tensile tests developed by Choi et al. was used in the present work. As such, the structure-property information from high strain rate tensile tests is potentially useful for models to predict the performance of sheet steel forming behavior and automotive crash response of components in the vehicle body.

This study is a continuation of extensive work by Pierce on Fe-22/25/28Mn-3Al-3Si steels [36]. More specifically, the stacking fault energies of these high-Mn steels were experimentally determined using weak-beam dark-field transmission electron microscopy (TEM) [14,37] and incorporated elastic constants measured by a novel combination of orientation imaging microscopy and nano-indentation [38]. The Fe-25Mn-3Al-3Si steel deforms by a combination of planar dislocation glide and secondary deformation mechanisms [4,13]. The SFE value of  $21 \pm 3 \text{ mJ/m}^2$  promotes twinning-induced plasticity as the dominant mode of secondary deformation with some evidence of transformation-induced plasticity in the form of hexagonal  $\epsilon$ -martensite [4]. When deformed at room temperature and quasi-static strain rates, these secondary deformation mechanisms contribute to high strain-hardening rates. Furthermore, Pierce et al. showed the influence of Mn-content and SFE on the mechanical properties of high-Mn steels and that an optimal SFE between 15 and  $39 \text{ mJ/m}^2$  produces the highest product of [ultimate tensile] strength and [total] elongation (PSE), due in large part to combined dislocation glide and secondary deformation, the latter producing obstacles to subsequent dislocation motion [4]. The present work focuses on understanding the effects of strain rate on the mechanical properties and deformation mechanisms in the austenitic microstructure of an Fe-25Mn-3Al-3Si (wt%) steel.

## 2. Experimental methods

### 2.1. Thermo-mechanical processing

The high-Mn alloy, [Fe-24.8Mn-2.99Al-3.03Si-0.019C-

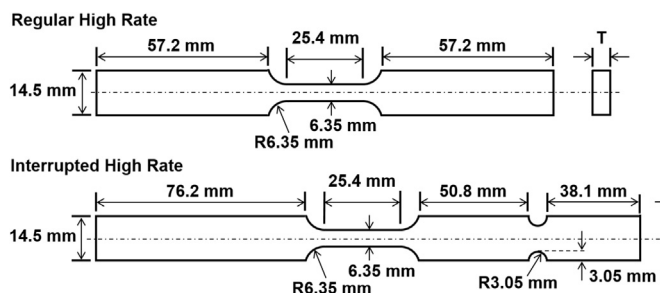


Fig. 1. Drawing of fabricated tensile specimens for failure and interruption at high strain rates, (T is sheet thickness), based on previous studies [35,40].

$< 0.0010 \text{ wt}\%$ ], was induction melted, cast into an ingot in Ar atmosphere and thermo-mechanically processed by hot rolling at  $1100^\circ\text{C}$  to 10 mm thick. This plate was sectioned in half to study different sheet thicknesses. The halves were further hot-rolled to 3.0 and 2.2 mm, respectively, then a 50% cold-rolled reduction was applied to create 1.5 and 1.1 mm thin sheets. These sheets were recrystallized for 0.5 h in air atmosphere at  $900^\circ\text{C}$ . Parallel plate grinding was used to remove the oxide scale and produced final sheet thicknesses of 1.15 and 0.95 mm. Samples for optical microscopy were prepared by mechanical polishing through 50 nm silica suspension followed by etching with a 10% nital solution. Grain size analysis using ASTM E112 [39] yielded a 21  $\mu\text{m}$  average grain size for both sheet thicknesses (1.15 mm and 0.95 mm). Thus, the 1.15 mm thick sheet has a slightly higher thickness-to-grain-size ratio.

### 2.2. Machining and servo-hydraulic tensile testing

Tensile specimens for elongation to failure and interruption were wire electro-discharge machined with dimensions as indicated in Fig. 1, based on specimen designs from Choi et al. and Addessio [35,40]. The 3.05 mm radius of the grip notches on the interruption geometry were further notched with a slow speed diamond saw blade to ensure interruption after the desired deformation in the gage section. Tensile testing was performed with a MTS 810 high-rate servo-hydraulic testing system. The system was comprised of a 500 kN capacity frame with a 50 kN capacity actuator. A 400 kN Kistler piezoelectric load washer was used to measure load. Data acquisition rates up to 2.5 MHz are attained through the National Instruments oscilloscope software program VirtualBench Scope™ and a National Instruments 12-bit data acquisition board with four data channels. A two-valve system and a slack adapter on the actuator allow the actuator to move at low and high rates. Strain was measured with a high elongation Vishay EP-08-250BG-120 strain gage adhered to the specimen with Vishay M-Bond A-12. However, the strain gage often detached prior to necking of the specimen as the strain gage is only rated up to a total strain of 0.2. For tests at  $\dot{\epsilon} = 2 \times 10^1 \text{ /s}$  and slower, the engineering strain rate prior to debonding was used to extrapolate the strain data to fracture. Total strain in every mechanical test was corroborated with caliper measurements of the gage length before and after tension testing. Specimens were strained in tension at various strain rates (from  $\dot{\epsilon} = 2 \times 10^{-4} \text{ /s}$  to  $\dot{\epsilon} = 2 \times 10^2 \text{ /s}$ ) either to failure or to specific strain levels using the interruption device and technique developed by Choi et al. [35].

### 2.3. Sample preparation for microstructural characterization and micro-hardness measurements

For transmission electron microscopy (TEM) sample preparation from the gage section of interrupted tensile specimens, 3 mm discs were wire electro-discharge machined orthogonal to the thickness dimension. To achieve electron transparency, these discs were mechanically polished to  $\sim 100 \mu\text{m}$  with SiC paper and electro-polished with a Struers TenuPol-5 twin jet system ( $-30^\circ\text{C}$ , 15 V, 80%  $\text{CH}_3\text{OH}$ , 20%

HNO<sub>3</sub> by volume). For scanning electron microscopy (SEM) sample preparation, 3 mm discs electro-discharge machined from gage sections were mounted in conductive bakelite. To achieve the preparation quality needed for high-resolution measurements in the SEM, (which are discussed in Section 2.6), the bulk samples were mechanically polished with SiC paper, auto-polished with 1  $\mu$ m diamond spray solution, etched for 20 s with 3% nital to chemically remove mechanical polishing effects and auto-polished through a 50 nm oxide polishing suspension, before final cleaning. Micro-hardness measurements were made on 3 mm discs of every deformed sample (which were prepared by the same methods for SEM imaging) with 32 indents per sample and 400  $\mu$ m spacing between indents, using an 800 g load on a Vickers micro-hardness machine. Samples for optical microscopy were prepared in the same manner as described for SEM preparation but also included an etching step after final polishing, (10% HNO<sub>3</sub> in 90% CH<sub>3</sub>OH by volume).

#### 2.4. Data acquisition at high strain rates

In the case of tests at  $\dot{\epsilon} = 2 \times 10^2$  /s, measurement of load and strain was performed with multiple methods. The engineering strain rate was higher than expected based on the actual displacement rate and resulted in extrapolated total elongation values up to  $\epsilon_{\text{eng.}} = 0.25$  greater than total elongation measured on the fractured tensile specimen with calipers. Therefore, for  $\dot{\epsilon} = 2 \times 10^2$  /s tests, actuator displacement rate was used instead to estimate strain after debonding of the strain gage. For tests faster than  $\dot{\epsilon} = 2 \times 10^1$  /s, the swift connection of the slack adapter generated mechanical resonance in the specimen and testing machine, which led to large oscillations in the load data, as seen in Supplementary Fig. S1. The load-ringing amplitude could be minimized by reducing the mass between the gage section and the load measuring device, which is why titanium grips were used [41,42]. Yang et al. suggest the use of two elastic strain gages to reduce load oscillations (one on either side of the grip section) during high strain rate tensile testing on a servo-hydraulic testing machine [43]. The load data from both strain gages is averaged and significantly reduces oscillation amplitude, as shown in Supplementary Fig. S2. Although this was not an option for all pull-to-failure tests, this concept was implemented in one test to check agreement of the hardware-based method suggested by Yang et al. with the software-based smoothing methods described below. The data reduction methods implemented in this work for the tests at  $\dot{\epsilon} = 2 \times 10^2$  /s comprise a moving average using MATLAB® (three iterations of smoothing for each data set), and spline fitting of the linear-elastic region and necking-fracture regions using Grapher™ software, as shown in Supplementary Fig. S3. Both the hardware and software-based smoothing methods provide satisfactory solutions to the problematic raw load washer data, as shown in Supplementary Fig. S4.

#### 2.5. High frame rate thermal imaging

Non-contact temperature measurements were collected during all mechanical tests with an infrared thermal camera (FLIR® A655sc) at a frame rate of 200 Hz (5 ms between frames), to produce a matrix with 640  $\times$  120-pixel resolution per frame. The calibration range of this device is  $-40$  to  $150$  °C, and within this range the overall accuracy of absolute temperature measurement is  $\pm 3$  °C. The maximum reading which could be displayed outside this calibrated range was  $160.2$  °C. To ensure consistent temperature measurements, the side of the gage section without a strain gage was coated with black spray paint [emissivity approximately equal to 1]. The camera had an unobstructed view of the specimen during testing. A large sheet of cardboard was placed behind the specimen during testing to achieve a uniform background. The absolute values of the non-contact temperature measurements were corroborated by measurements made with a thermocouple that was resistance-welded to the other side of a tensile specimen

during a practice test.

#### 2.6. Characterization of planar defects

To quantitatively characterize the effects of strain rate on changes in the distribution of planar defects, (especially twins and epsilon martensite), both SEM and TEM-based characterization techniques have been utilized by others [44–49,58,59,61]. Such characterization techniques are used to quantify the thickness and spacing of planar defects, (see Supplementary Fig. S5 and Supplementary Fig. S6) and include electron back-scattered diffraction (EBSD), electron channeling contrast imaging (ECCI), and conventional dark-field transmission electron microscopy (DF-TEM). To minimize as many variables as possible in quantifying planar defects, the microscopy work discussed in this section is based on tensile specimens of the same sheet thickness (1.15 mm). Micro-hardness indents were placed in a grid on polished SEM samples to act as markers during imaging. EBSD on a field emission SEM (JEOL JSM 6500F) at 25 kV was used to survey grains with  $< 101 >$  orientations parallel to the beam direction. For those properly oriented grains, ECCI on a field emission SEM (Zeiss Merlin) at 30 kV was used to first survey for proper channeling conditions, record at medium-high magnification a slow scan image revealing the planar defects. Supplementary Fig. S5 shows example images recorded on the different microscopes. Suitable DF-TEM diffracting conditions were achieved with a TEM (FEI Tecnai Osiris) at 200 kV by first surveying grains with convergent beam electron diffraction (CBED) and orienting them to a  $< 101 >$  beam direction, followed by selecting the appropriate extra reflections (twinning or  $\epsilon$ -martensite) in selected area electron diffraction (SAED) with a sufficiently small (10  $\mu$ m) objective aperture to produce an unambiguous DF image (Supplementary Fig. S6). An image-processing recipe [FFT filter, adaptive threshold, black-white inversion, feature rejection and watershed] was used to segment planar defects from a given image using MIPAR software [50]. Approximately 100 lines were drawn perpendicular to the segmented defects and used to count the thickness of and spacing between all planar defects in a given image.

### 3. Results

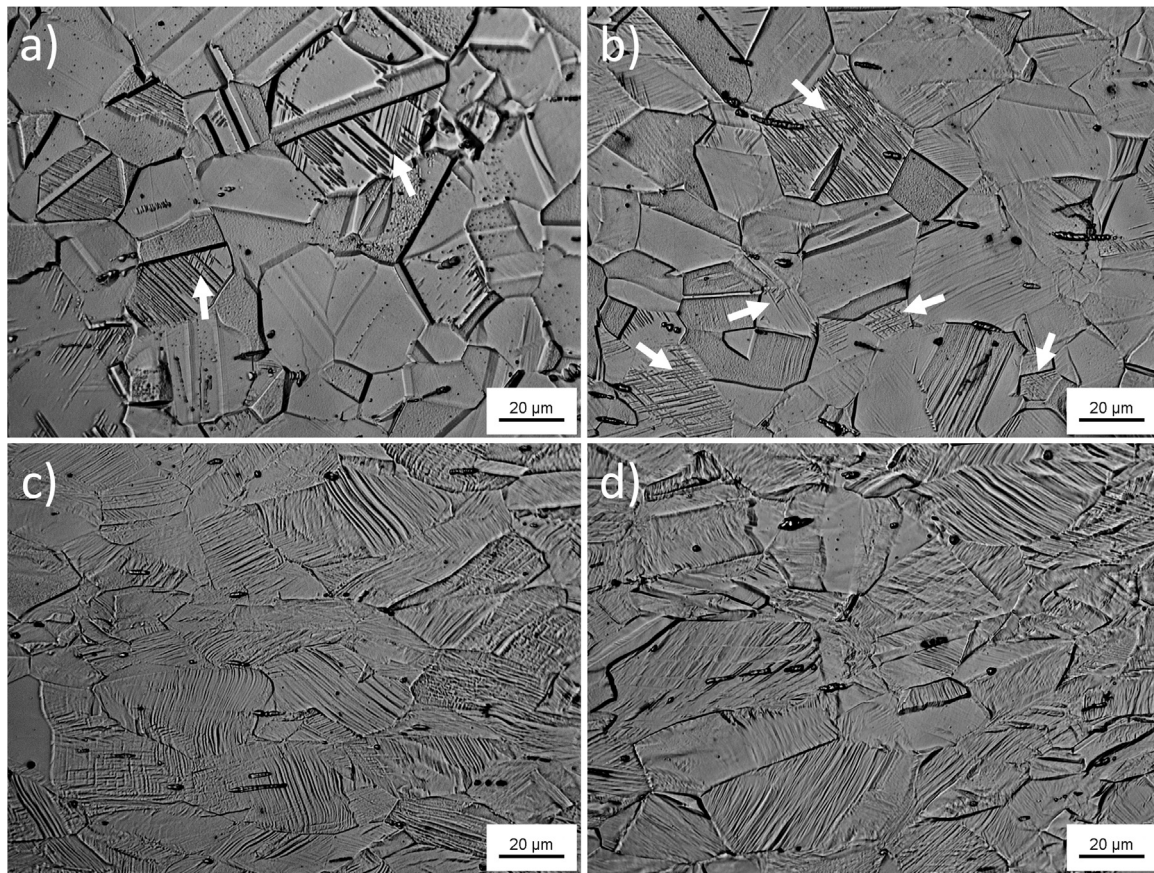
#### 3.1. Optical microscopy

Fig. 2 shows optical micrographs of the deformed microstructure for interrupted and pulled-to-failure tensile tests at various strain rates. For Fig. 2a, the tensile test at  $\dot{\epsilon} = 2 \times 10^2$  /s was interrupted at  $\epsilon_{\text{eng.}} = 0.07$ . Although TEM is required to differentiate between mechanical twins and/or epsilon martensite laths, Fig. 2a clearly reveals planar defects in a few grains and in some instances, multiple variants (as indicated by arrows). After interruption at  $\epsilon_{\text{eng.}} = 0.2$  at the same strain rate, ( $\dot{\epsilon} = 2 \times 10^2$  /s), planar defects are apparent in most grains, (as seen in Fig. 2b), in conjunction with more frequent instances of multiple variants (as indicated by arrows). The micrographs in Fig. 2c-d originate from areas in the uniformly elongated region of the gage section that are far from the fracture surfaces of tensile samples pulled-to-failure. The microstructures in specimens deformed to failure at  $\dot{\epsilon} = 2 \times 10^{-4}$  /s and  $\dot{\epsilon} = 2 \times 10^2$  /s (Fig. 2c-d, respectively) are qualitatively the same. In general, most grains show evidence of planar defects (mechanical twins and/or epsilon martensite laths) distributed throughout the entire grain in at least one variant. The accommodation of large amounts of engineering strain by multiple slip systems is highlighted by substantial curvature of planar features and shearing within each of the elongated grains.

#### 3.2. Influence of strain rate and specimen thickness on mechanical properties

An important criterion for AHSS design involves maximizing the





**Fig. 2.** Optical micrographs of the Fe-25Mn-3Al-3Si alloy a) tested at  $\dot{\epsilon} = 2 \times 10^2$  /s and interrupted at  $\epsilon_{\text{eng.}} = 0.07$ , b) tested at  $\dot{\epsilon} = 2 \times 10^2$  /s and interrupted at  $\epsilon_{\text{eng.}} = 0.2$ , c) deformed to failure ( $\epsilon_{\text{eng.}} = 0.62$ ) at  $\dot{\epsilon} = 2 \times 10^{-4}$  /s and d) deformed to failure ( $\epsilon_{\text{eng.}} = 0.60$ ) at  $\dot{\epsilon} = 2 \times 10^2$  /s. In parts a) and b) grains with multiple variants of mechanical twins and/or hexagonal epsilon martensite laths are indicated by arrows. All samples etched for 20 s with 10% nital. The tensile axis is in the horizontal direction.

strain at instability, i.e. the amount of uniform strain. This instability is derived from the Considère criterion and is defined as the true strain at which the strain-hardening rate is equal to the true stress [51,52]. Fig. 3a shows the representative engineering stress-strain curves for the 0.95 mm sheet thickness at strain rates in the range of  $\dot{\epsilon} = 2 \times 10^{-2}$  to  $\dot{\epsilon} = 2 \times 10^2$  /s and Fig. 3b shows the representative engineering stress-strain curves for the 1.15 mm sheet thickness at strain rates in the range of  $\dot{\epsilon} = 2 \times 10^{-4}$  to  $\dot{\epsilon} = 2 \times 10^2$  /s. All engineering stress-strain curves can be found in the supplementary section (see Supplementary Fig. S1). Representative true stress-strain curves and corresponding strain-hardening rates were calculated from engineering stress-strain values up to the point of instability and are shown in Fig. 4a for the 0.95 mm sheet thickness and in Fig. 4b for the 1.15 mm thick sheet. The true stress-strain values which satisfy the instability condition are converted to engineering stress-strain values of ultimate tensile strength (UTS) and uniform elongation (UE) and summarized in Fig. 5 as a function of strain rate. Values of the 0.2% offset yield strength (YS) and total elongation (TE) from the representative engineering stress-strain curves in Fig. 3 are also summarized in Fig. 5 as a function of strain rate. Fig. 5a illustrates the behavior of the YS and UTS for the 0.95 mm sheet thickness as a function of strain rate, while Fig. 5c displays the change in YS and UTS as a function of strain rate for the 1.15 mm sheet thickness. Fig. 5b shows the effect of strain rate on UE and TE values for the 0.95 mm sheet thickness, while Fig. 5d demonstrates the effect of strain rate on UE and TE for the 1.15 mm sheet thickness.

The 0.2% offset yield strength of the 1.15 mm thick sheet rose continuously from  $306 \pm 10$  MPa to  $503 \pm 10$  MPa (a 64% increase) with increasing strain rate by 6 orders of magnitude from  $\dot{\epsilon} = 2 \times 10^{-4}$  to  $\dot{\epsilon} = 2 \times 10^2$  /s, (see Figs. 3b and 5c). As for the 0.95 mm thick sheet, increasing strain rate by 4 orders of magnitude from  $\dot{\epsilon} = 2 \times 10^{-2}$  to  $\dot{\epsilon} = 2 \times 10^2$  /s resulted in an increase of the 0.2% offset yield strength

from  $394 \pm 18$  MPa to  $502 \pm 10$  MPa (a 27% increase), as seen in Figs. 3a and 5a. For comparison, the 0.2% offset yield strength of the 1.15 mm thick sheet specimen deformed at  $\dot{\epsilon} = 2 \times 10^{-2}$  /s was 395 MPa, which also yields an increase of 27% from  $\dot{\epsilon} = 2 \times 10^{-2}$  to  $\dot{\epsilon} = 2 \times 10^2$  /s. Therefore, the different sheet thicknesses had no influence on the magnitude of the 0.2% offset yield strength or the strain rate sensitivity of the yield strength.

An increase in the instantaneous engineering stress, (of  $> 100$  MPa), at any given strain occurs with increasing the strain rate from  $\dot{\epsilon} = 2 \times 10^{-2}$  to  $\dot{\epsilon} = 2 \times 10^2$  /s, regardless of sheet thickness (see Fig. 3a-b). Truly quasi-static strain rate tests ( $\dot{\epsilon} = 2 \times 10^{-4}$  /s in this case) were only conducted with the 1.15 mm thick sheet, seen in Fig. 3b, and the results show greater work-hardening, plus a higher UTS and TE as compared to the  $\dot{\epsilon} = 2 \times 10^{-2}$  /s test of the same sheet thickness. The PSE of the 0.95 mm thick sheet increased from 33,000 MPa% to 44,000 MPa% with increasing the strain rate from  $\dot{\epsilon} = 2 \times 10^{-2}$  to  $\dot{\epsilon} = 2 \times 10^2$  /s. The same increase in strain rate for the 1.15 mm thick sheet yielded an increase in PSE from 44,000 MPa% to 58,000 MPa%. As a baseline measurement for PSE comparisons, the quasi-static PSE of the 1.15 mm thick sheet is 48,000 MPa%. Thus, increasing the strain rate from  $\dot{\epsilon} = 2 \times 10^{-2}$  to  $\dot{\epsilon} = 2 \times 10^2$  /s increases the PSE and increasing sheet thickness increases the PSE of the Fe-25Mn-3Al-3Si alloy.

In the case of the 1.15 mm sheet thickness, Fig. 3b shows that the flow stress of the  $\dot{\epsilon} = 2 \times 10^{-2}$  /s test, for strain values below approximately  $\epsilon_{\text{eng.}} = 0.2$ , was greater for the quasi-static test ( $\dot{\epsilon} = 2 \times 10^{-4}$  /s). Differences in the strain-hardening rate (shown in Fig. 4b) lead to a slightly smaller TE and UE, (by approximately  $\epsilon_{\text{eng.}} = 0.03$ ), for the test at  $\dot{\epsilon} = 2 \times 10^{-2}$  /s and a slightly larger UTS, (by

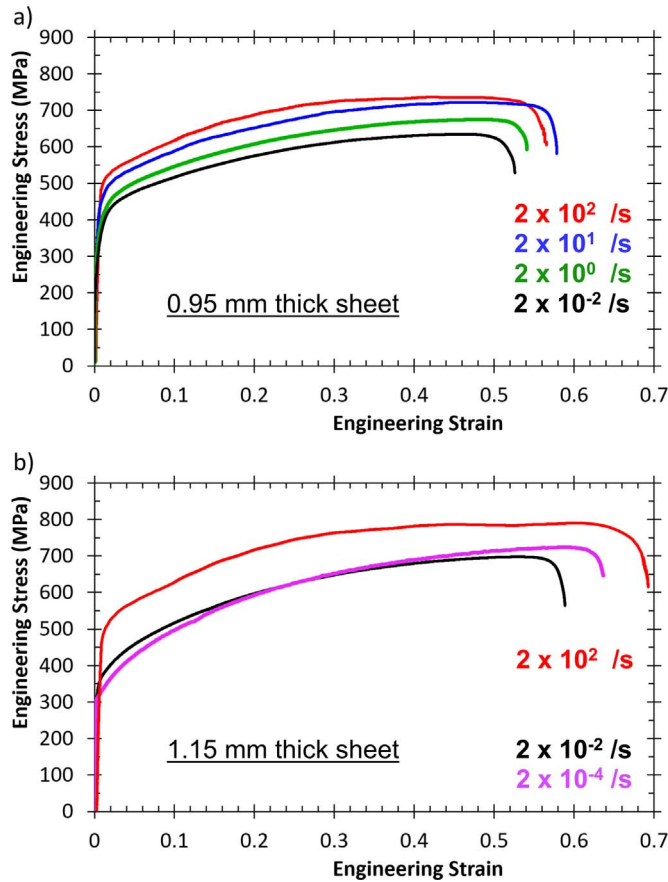


Fig. 3. Representative engineering stress (MPa) vs. engineering strain curves for the Fe-25Mn-3Al-3Si alloy when pulled-to-failure at strain rates from  $\dot{\epsilon} = 2 \times 10^{-4}$  /s to  $\dot{\epsilon} = 2 \times 10^2$  /s, based on: a) specimens from the 0.95 mm thick sheet and b) specimens from the 1.15 mm thick sheet.

approximately 50 MPa), for the quasi-static tests ( $\dot{\epsilon} = 2 \times 10^{-4}$  /s). These observations equate to a slight decrease in PSE between  $\dot{\epsilon} = 2 \times 10^{-4}$  /s and  $\dot{\epsilon} = 2 \times 10^{-2}$  /s. Within the context of the strain-hardening behaviors in Fig. 4, the lowest value of strain-hardening rate below  $\epsilon_{\text{true}} = 0.15$  is observed for the tests at  $\dot{\epsilon} = 2 \times 10^{-2}$  /s, regardless of sheet thickness. The [quasi-static] test at  $\dot{\epsilon} = 2 \times 10^{-4}$  /s of the 1.15 mm thick sheet has a greater strain-hardening rate than the test at  $\dot{\epsilon} = 2 \times 10^{-2}$  /s, but a lower yield strength. As strain rate is increased from  $\dot{\epsilon} = 2 \times 10^{-2}$  /s to  $2 \times 10^2$  /s, the strain-hardening rate between  $\epsilon_{\text{true}} = 0.07$  and  $0.15$  increases slightly by  $> 200$  MPa. However, given the limited number of tensile tests conducted with the 1.15 mm sheet thickness, strict conclusions should not be drawn from these observations.

The average TE increases by less than 10% engineering strain across the entire range of strain rates for the 0.95 mm sheet thickness, as shown in Fig. 5b. There is little change in UE with increasing strain rate up to  $\dot{\epsilon} = 2 \times 10^1$  /s, and UE decreases between  $\dot{\epsilon} = 2 \times 10^1$  /s and  $\dot{\epsilon} = 2 \times 10^2$  /s, (see Fig. 5b). The data for the 1.15 mm thick sheet show that an increase in strain rate from  $\dot{\epsilon} = 2 \times 10^{-4}$  to  $\dot{\epsilon} = 2 \times 10^2$  /s increases YS significantly and UTS slightly, (see Fig. 5c), whereas UE decreases, (see Fig. 5d). Between  $\dot{\epsilon} = 2 \times 10^{-4}$  and  $\dot{\epsilon} = 2 \times 10^{-2}$  /s, TE decreases slightly and then increases by nearly 10% strain between  $\dot{\epsilon} = 2 \times 10^{-2}$  and  $\dot{\epsilon} = 2 \times 10^2$  /s for the 1.15 mm sheet thickness. As seen in Fig. 5b and d, the average uniform elongation and average ultimate tensile strength is slightly greater for the 1.15 mm sheet thickness, (for tests deformed at the same strain rate:  $\dot{\epsilon} = 2 \times 10^{-2}$  /s and  $\dot{\epsilon} = 2 \times 10^2$  /s). However, when one standard deviation is taken into account for the multiple tests with 0.95 mm sheet thickness and compared to the 1.15 mm sheet thickness results, (which are based on only

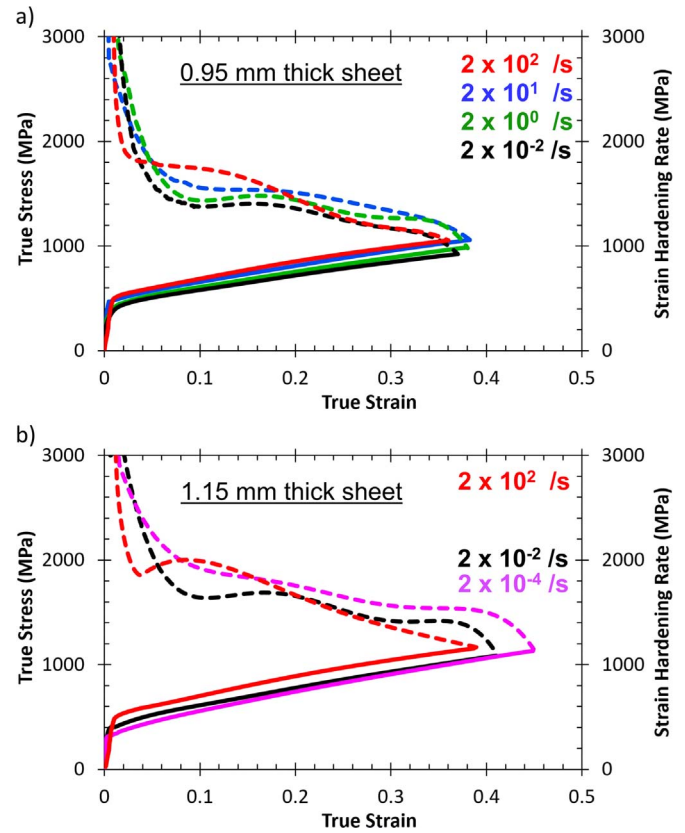


Fig. 4. Representative true stress (MPa) and strain-hardening rate (MPa) vs. true strain for the Fe-25Mn-3Al-3Si alloy when pulled-to-failure at strain rates from  $\dot{\epsilon} = 2 \times 10^{-4}$  /s to  $\dot{\epsilon} = 2 \times 10^2$  /s, based on: a) specimens from the 0.95 mm thick sheet and b) specimens from the 1.15 mm thick sheet. The Considère criterion was used to determine the instability condition, such that these true stress-strain curves end at the point where the strain-hardening rate curve intersects the true stress-strain curve.

one tensile test each at  $\dot{\epsilon} = 2 \times 10^{-2}$  /s and  $\dot{\epsilon} = 2 \times 10^2$  /s), it is concluded that uniform elongation and ultimate tensile strength do not differ significantly between the studied sheet thicknesses.

Fig. 5b and d also show that an increase in sample thickness (of approximately 10%) increased total elongation by approximately 10% (for tests deformed at the same strain rate,  $\dot{\epsilon} = 2 \times 10^{-2}$  /s and  $\dot{\epsilon} = 2 \times 10^2$  /s). Reduction-in-area was also considered and measured at the smallest region of the neck of the fracture point with calipers. Supplementary Fig. S7 shows reduction-in-area measurements on all tensile samples for both thicknesses. The 1.15 mm thick sheet specimens had slightly higher reduction-in-area than the 0.95 mm thick sheet specimens, but reduction-in-area measurements on sheet specimens are more difficult than on cylindrical samples and can lead to large inaccuracies. In summary of Supplementary Fig. S7, quasi-static strain rates showed the highest reduction-in-area, but reduction-in-area values for strain rates of  $\dot{\epsilon} = 2 \times 10^{-2}$  /s to  $\dot{\epsilon} = 2 \times 10^2$  /s do not show any significant difference for the same sheet thickness. Therefore, the TE, UE and reduction-in-area values suggest that post-uniform elongation and/or more diffuse necking (longer necks and/or multiple necks) is more prevalent at higher strain rates.

### 3.3. Micro-hardness measurements

The micro-hardness was measured for specimens in the as-recrystallized state and following both interrupted and pull-to-failure tests to determine if any significant differences exist in the material hardness after deformation at different strain rates for the same nominal strain. Any differences in the micro-hardness with respect to a change in strain and/or strain rate might be attributed to changes in the



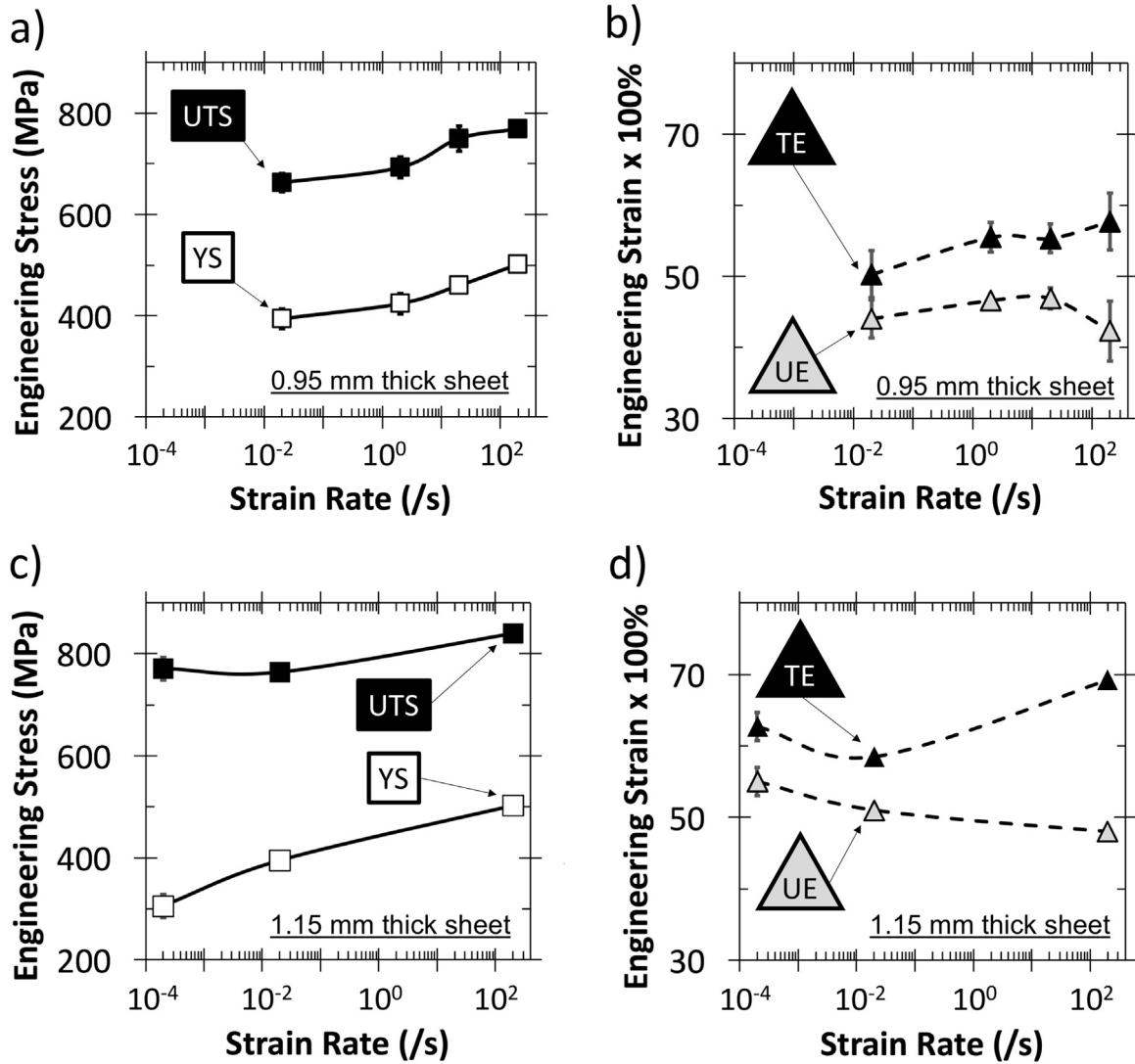


Fig. 5. a) and c) Ultimate tensile strength (UTS) and 0.2% offset yield strength (YS) values, along with b) and d) total elongation (TE) and uniform elongation (UE) values are summarized as a function of strain rate for a-b) 12 specimens from the 0.95 mm thick sheet and c-d) 4 specimens from the 1.15 mm thick sheet. Error bars represent one standard deviation. Data points without error bars are based on only one pull-to-failure test for that strain rate and sheet thickness.

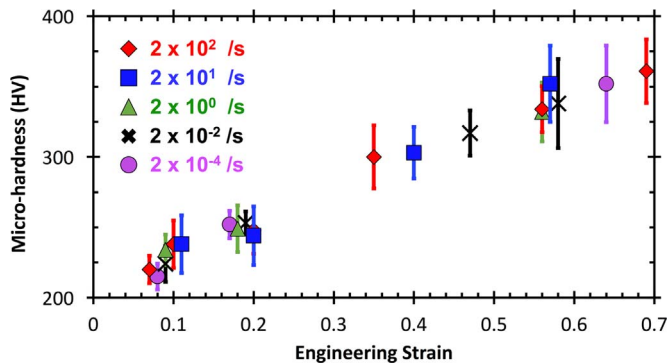


Fig. 6. Micro-hardness measurements completed for all interrupted and pull-to-failure samples and plotted as a function of engineering strain, for all strain rates. Error bars represent one standard deviation based on an average of all hardness indents made for a given strain rate and strain.

microstructure, including differences in dislocation density, dislocation sub-structure, and the type, spacing, and amount of planar secondary deformations mechanisms. The grain size is  $21 \mu\text{m}$  for both sheet thicknesses (1.15 mm and 0.95 mm). The hardness of the as-

recrystallized 0.95 mm and 1.15 mm thick sheets were  $151 \pm 15$  HV and  $160 \pm 19$  HV, respectively. As no statistically significant difference in micro-hardness for the as-received microstructures existed, the measurements on both steel sheets are plotted together. Fig. 6 clearly shows an increase in Vickers micro-hardness with increasing engineering strain, (from approximately 155 HV in the as-received condition to approximately 350 HV after pull-to-failure). However, Vickers measurements of all interrupted and pull-to-failure samples do not indicate a significant difference in micro-hardness with respect to a difference in strain rate at nominally the same level of strain. This could indicate that 1) no significant differences in the microstructure exist at different strain rates for the same nominal strain, or 2) that any microstructural differences that exist do not significantly influence the hardness.

### 3.4. Non-contact temperature measurements

Fig. 7a-b depicts thermal images recorded using a calibrated thermal camera at specific time/strain intervals during tensile tests conducted at engineering strain rates of a)  $\dot{\epsilon} = 2 \times 10^{-2}$  /s and b)  $\dot{\epsilon} = 2 \times 10^1$  /s. At both strain rates the temperature distribution in the gage section was approximately uniform at 0.21 strain. However, the images

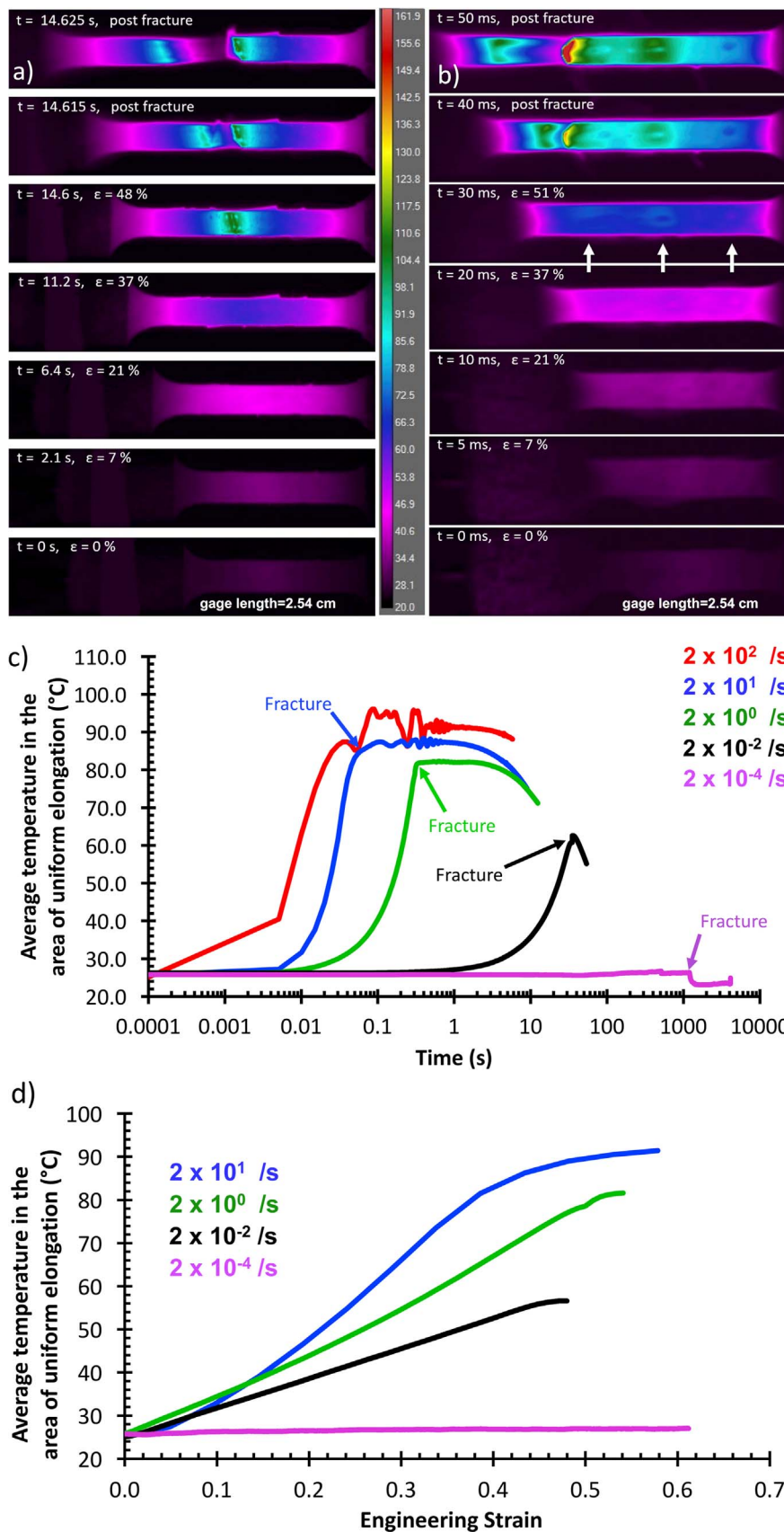


Fig. 7. a, b) Thermal images recorded at 200 fps by an infrared camera as a function of strain, with indicated time stamps corresponding to different strain rates: a)  $\dot{\epsilon} = 2 \times 10^{-2} /s$  and b)  $\dot{\epsilon} = 2 \times 10^1 /s$ . The arrows in b) indicate localized hot-spots, (multiple necking initiation points), with the left-most being the eventual fracture surface. c) Non-contact measurements of the average surface temperature along the gage length are plotted as a function of time for the different strain rates for representative pull-to-failure tests. d) Average surface temperature of uniformly elongated regions during representative pull-to-failure tensile tests of the Fe-25Mn-3Al-3Si alloy.

immediately following fracture show that localized heating on the order of 110 °C occurred in a single neck location for  $\dot{\epsilon} = 2 \times 10^{-2}$  /s. In comparison, the temperature distribution of the  $\dot{\epsilon} = 2 \times 10^1$  /s sample shows several localized areas of significantly higher temperature, which suggests multiple areas of strain localization. The appearance of multiple regions of strain localization was observed in several instances for the  $\dot{\epsilon} = 2 \times 10^1$  /s and  $\dot{\epsilon} = 2 \times 10^2$  /s tests, (another example is provided in Fig. S8). The average temperature of the localized heat patterns registered 26 °C higher as compared to the rest of the uniformly deformed gage section. The appearance of multiple strain localizations at the higher strain rate supports the increase in post-uniform necking at higher strain rates, whereas reduction-in-area (at the smallest region of neck) is constant with an increase in strain rate from  $\dot{\epsilon} = 2 \times 10^{-2}$  /s to  $\dot{\epsilon} = 2 \times 10^2$  /s. The fracture area of a given test was observed to be significantly hotter than the uniformly elongated gage, as expected for the large energy release associated with the creation of the free surfaces. Further, the strain rate in the neck increases because of the localization of strain. A maximum spot temperature near the fracture surface was measured to be approximately 160 °C for a tensile specimen deformed at  $\dot{\epsilon} = 2 \times 10^1$  /s. The temperature of such locations most likely exceeded this value in some of the tests, but the camera could not accurately record temperature too far outside the calibration range of –40 to 150 °C. After fracture, the average sample temperature continued to rise slightly by approximately 5 °C. This temperature rise post fracture may be attributed to thermal equilibration of the sample. More heat is likely generated at the mid-thickness of the sample than at the free surface during plastic deformation, resulting in conductive heat transfer to the free surface during the test. Consequently, the data obtained from the thermal camera may slightly underestimate the average temperature of the specimen at any specific strain/time interval during the test, especially for higher strain rates tests.

ResearchIR™ software was used to calculate the average surface temperature across the entire area of the gage length, neglecting the necked region and fracture surface, for every mechanical test. As sample thickness did not influence temperatures by more than 2 °C for a given strain rate, the average temperatures from representative pull-to-failure tests for the 0.95 mm and 1.15 mm thick sheets are plotted together in Fig. 7c. Fluctuations in temperature measurement after fracture of samples deformed at  $\dot{\epsilon} = 2 \times 10^1$  and  $\dot{\epsilon} = 2 \times 10^2$  /s are due to the sample moving laterally with the load train outside of the defined area of the stationary thermal camera. The sharp increase in specimen temperature at 0.005 s for the tests at  $\dot{\epsilon} = 2 \times 10^2$  /s is because the thermal camera could only record up to 200 fps, (a frame captured every 5 ms), so only one image was recorded before fracture for the  $\dot{\epsilon} = 2 \times 10^2$  /s tests as seen in Supplementary Fig. S8. After fracture of the tensile specimen, the average surface temperature along the gage length, neglecting the necked region and fracture surface, was approximately  $91 \pm 5$  °C for the tests at  $\dot{\epsilon} = 2 \times 10^2$  /s, representing an increase in temperature of approximately 65 °C. The increase in strain rate from  $\dot{\epsilon} = 2 \times 10^1$  to  $\dot{\epsilon} = 2 \times 10^2$  /s resulted in an increase in average temperature of only 6 °C, which should be proportional to the difference in work put into the sample minus the heat dissipated by the grips and surrounding air at the two different strain rates [23]. For the  $\dot{\epsilon} = 2 \times 10^0$  /s,  $\dot{\epsilon} = 2 \times 10^1$  /s, and  $\dot{\epsilon} = 2 \times 10^2$  /s tests the average temperature after fracture was 82, 85, and 91 °C, respectively. Under adiabatic heating conditions, the amount of heating is proportional to the amount of plastic work [53,23]. As shown in Table 1, the area under the engineering stress-strain curve, based on results in Fig. 3, increases with increasing strain rate, (not including quasi-static strain rates where heating is negligible). The expected temperature rise under fully adiabatic conditions was calculated using an accepted formula for estimating temperature rise during measured plastic work including a 90% efficiency in conversion of mechanical energy to heat energy and a heat capacity of 0.46 kJ/(kg K) [15,56]. The mass density used in the calculations for the Fe-25Mn-3Al-3Si steel is 7.4 g/cm<sup>3</sup> [36]. The trend in calculated results are consistent with the trend in experimental

**Table 1**

Average area under engineering stress strain curves from Fig. 3, (numerically-integrated) and predicted [15,56] increase in temperature.

Strain rate (/s)	0.95 mm thick sheets Average (area under engineering stress-strain curve) and the [predicted temperature] under the assumption of adiabatic conditions. (mJ/mm <sup>3</sup> ) / [°C]	1.15 mm thick sheets Average (area under engineering stress-strain curve) and the [predicted temperature] under the assumption of adiabatic conditions. (mJ/mm <sup>3</sup> ) / [°C]
$2 \times 10^2$	388 / 94	501 / 122
$2 \times 10^1$	354 / 86	–
$2 \times 10^0$	330 / 80	–
$2 \times 10^{-2}$	283 / 69	358 / 87

observations, (described in more detail with reference to Fig. 7d), such that the average temperature in the uniformly elongated area increases with increasing strain rate. Lastly, the  $\dot{\epsilon} = 2 \times 10^2$  /s and  $\dot{\epsilon} = 2 \times 10^1$  /s tests seemed to exhibit a wider spread in maximum average temperature across the elongated gage section, (neglecting the fracture surface), as compared to the lower strain rate tests.

The average surface temperature in the area of uniform elongation is plotted as a function of strain for representative curves in Fig. 7d. The 200/s data is not included in the plot, because only one image was recorded before fracture. Fig. 7d confirms that as strain accumulates and strain rate increases, (from  $\dot{\epsilon} = 2 \times 10^{-2}$  to  $\dot{\epsilon} = 2 \times 10^1$  /s), the average surface temperature of the gage length (where it deforms uniformly) increases. The calculated results in Table 1, (based on measured plastic work under the assumption of adiabatic heating conditions), predicts a temperature of 80 °C for the  $\dot{\epsilon} = 2 \times 10^0$  /s tests, which is consistent with the temperature measured right before fracture during the  $\dot{\epsilon} = 2 \times 10^0$  /s tests, seen in Fig. 7d. Also seen in Fig. 7d, the specimen temperature curves at  $\dot{\epsilon} = 2 \times 10^0$  and  $\dot{\epsilon} = 2 \times 10^1$  /s exhibit some overlap, suggesting that near-adiabatic heating conditions are reached for strain rates at or greater than  $\dot{\epsilon} = 2 \times 10^0$  /s.

### 3.5. Thermodynamic modeling of stacking fault energy

A composition- and temperature-dependent thermodynamic model was previously developed to predict the SFE of Fe-Mn-Al-Si steels [14]. This model was used in the current work to assess the increase in SFE as a function of strain and temperature and the results are reported in Tables 2 and 3, respectively. The model calculates the SFE on the basis of the difference in Gibbs free energy of the face-centered cubic (FCC) and hexagonal close-packed (HCP) phases, the interfacial energy between the FCC and HCP phases, as well as the strain energy that arises due to a contraction in molar volume of the HCP phase [14]. The exact temperature dependence of the FCC/HCP interfacial energy is unknown and for the purposes of this calculation, the FCC/HCP interfacial energy of 8.6 mJ/m<sup>2</sup> determined at room temperature (RT) for a Fe-25Mn-3Al-3Si steel of nearly the same actual composition is assumed. However, Cotes et al. [54] reported that the FCC/HCP interfacial energy decreases with increasing temperature in binary Fe-Mn steels. In addition, the

**Table 2**

Predicted stacking fault energy with respect to an increase in temperature due to adiabatic heating for three interrupted tests & an average temperature of the four pulled-to-failure tests (average total strain of 0.58) when deformed at the same strain rate.

Total strain ( $\epsilon_{\text{eng}}$ )	Average temperature in the uniformly elongated area when deformed at $\dot{\epsilon} = 2 \times 10^1$ /s (°C)	Predicted SFE (mJ/m <sup>2</sup> )
0.58	91.1	35.3
0.40	59.9	30.1
0.18	41.8	27.2
0.11	37.8	26.6



**Table 3**

Predicted stacking fault energy with respect to an increase in temperature due to adiabatic heating when interrupted to  $\epsilon_{\text{eng.}} = 0.2$  at different strain rates.

Strain rate (/s)	Average temperature in the uniformly elongated area interrupted to $\epsilon_{\text{eng.}} = 0.18$ (°C)	Predicted SFE (mJ/m <sup>2</sup> )
$2 \times 10^2$	43.9	27.6
$2 \times 10^1$	41.8	27.2
$2 \times 10^0$	39.1	26.8
$2 \times 10^{-2}$	36.3	26.4
$2 \times 10^{-4}$	26.7	25.1

strain energy term, calculated to be 2.3 mJ/m<sup>2</sup> at room temperature is also assumed to be independent of temperature in the calculation of the SFE. However, the dependence of the strain energy term on shear modulus, which is reported to decrease with increasing temperature in high Mn steels [55], suggests the strain energy term might also decrease with increasing temperature. Therefore, the calculated SFEs may slightly overestimate the actual SFEs of the material at elevated temperatures. Table 2 shows the predicted SFE for samples deformed at  $\dot{\epsilon} = 2 \times 10^1$  /s to various amounts of strain based on three interruption tests and one pull-to-failure test. The model predicts that the SFE increases from a RT value of approximately 21 [14] to 35.3 mJ/m<sup>2</sup> at maximum uniform elongation of a test at  $\dot{\epsilon} = 2 \times 10^1$  /s corresponding to a temperature of 91 °C. Table 3 shows the predicted SFE for samples interrupted at  $\epsilon_{\text{eng.}} = 0.2$  in the strain rate range of  $\dot{\epsilon} = 2 \times 10^{-4}$  to  $\dot{\epsilon} = 2 \times 10^2$  /s. An increase of 6 orders of magnitude in strain rate from  $\dot{\epsilon} = 2 \times 10^{-4}$  to  $\dot{\epsilon} = 2 \times 10^2$  /s only increases the average specimen temperature by only 17 °C and the SFE by only 3 mJ/m<sup>2</sup> for two samples interrupted at  $\epsilon_{\text{eng.}} = 0.2$ .

### 3.6. TEM for characterizing planar defects in interrupted samples

The onset of strain-induced mechanical twinning and/or epsilon martensite is often manifested by the appearance of a change in shape, usually between  $\epsilon_{\text{true}} = 0.1$  and 0.2, of the strain-hardening rate versus true strain curve at quasi-static strain rates [4]. Therefore, changes in the strain-hardening rate at high strain rates may indicate a difference in twin volume fraction or a change in the strain at which mechanical twinning begins [23] relative to quasi-static strain rates. In previous work on this high-Mn alloy using different tensile geometries [8,15,4], characterization of the evolution of dislocation structures during deformation at quasi-static strain rates indicated a TWIP-dominated behavior, with some evidence of TRIP in the form of hexagonal  $\epsilon$ -martensite. As shown in the bright-field TEM micrograph in Fig. 8, a specimen interrupted at  $\epsilon_{\text{eng.}} = 0.1$  tested at  $\dot{\epsilon} = 2 \times 10^2$   $\epsilon$ /s in the present work exhibits mechanical twinning. The mechanical twins are clearly impeding the glide of other partial dislocations on non-coplanar slip systems. Twins and epsilon martensite have been reported to form even before  $\epsilon_{\text{eng.}} = 0.1$  for this alloy at quasi-static strain rates [4], so it is no surprise that the planar defects present at  $\epsilon_{\text{eng.}} = 0.1$  are observed to impede motion of leading partial dislocations [56] on different slip systems. More importantly, an increase in strain-hardening may also arise from a decrease in dislocation mean free path by an increase in forest dislocation density or decrease in the average spacing between planar defects. After interruption at  $\epsilon_{\text{eng.}} = 0.2$  for a specimen tested at  $\dot{\epsilon} = 2 \times 10^2$   $\epsilon$ /s, (see Fig. 9), both TWIP and TRIP effects are observed on parallel {111} slip systems. This observation indicates hexagonal  $\epsilon$ -martensite can still form at high strain rates, despite an increase in the SFE due to adiabatic heating. Moreover, the overall message gathered from Figs. 8 and 9 is that there are no significant changes in the underlying TWIP-TRIP mechanisms between  $\dot{\epsilon} = 2 \times 10^{-4}$   $\epsilon$ /s and  $\dot{\epsilon} = 2 \times 10^2$   $\epsilon$ /s because the microstructural evolution is similar, (TWIP-dominated behavior with some evidence of TRIP in the form of hexagonal  $\epsilon$ -martensite). These observations will be quantified and

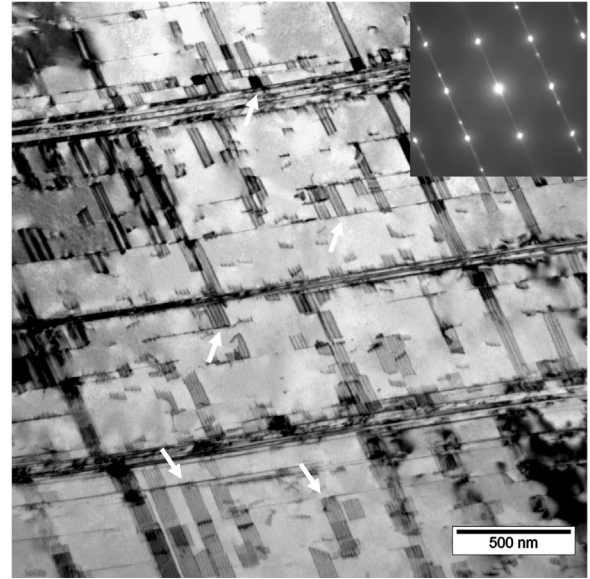
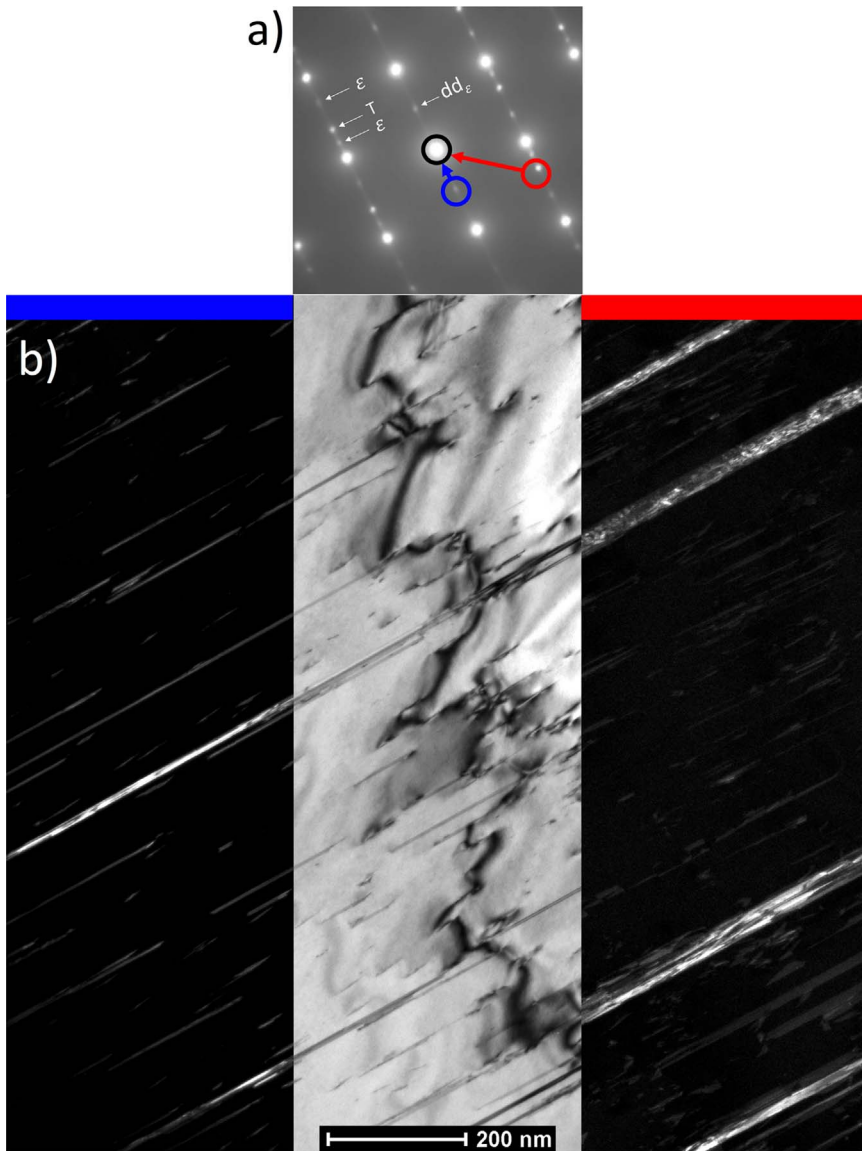


Fig. 8. The inset selected area electron diffraction pattern (SAEDP) was recorded at the [110] zone axis to identify the edge-on planar defects, (in this case: deformation twinning), in a 0.95 mm sheet specimen interrupted at  $\epsilon_{\text{eng.}} = 0.1$  and tested at  $\dot{\epsilon} = 2 \times 10^2$  /s. By tilting the sample slightly off the zone axis, a two-beam condition using a 1 – 1 – 1 diffracting (g)-vector to provide greater defect contrast was created for the bright field image, which highlights the ability of some planar defects to impede subsequent partial dislocation motion along other {111}/ <110> slip systems, as indicated by white arrows.

discussed in the proceeding section with the implication that slight differences in strain-hardening rate for the Fe-25Mn-3Al-3Si (wt%) alloy are not associated with a transition from TRIP-dominated to TWIP-dominated behavior, but rather due to slight changes in dislocation mean free path.

### 3.7. Quantification of planar defects

SEM and TEM-based characterization techniques were used to quantify the thickness and spacing of planar defects in tensile specimens interrupted at different strain rates. DF-TEM measurements of epsilon martensite thickness revealed 94% of the population is grouped at 10 nm and smaller. Kernel fitting of planar defect thickness distributions acquired by ECCI and DF-TEM, seen in Fig. S9, shows that distributions acquired by ECCI measurements tend to miss most of the planar defects that are less than 10 nm in thickness for this alloy. It should be noted that ECCI doesn't differentiate between twins and epsilon martensite. Although some surveyed grains contained a higher number of planar defects and other grains contained fewer planar defects, representative images are shown in Fig. 10. As the distributions are non-Gaussian, both the average thickness and median thickness for a given distribution are reported in Figs. 11. Table 4 indicates an approximately 50% chance of surveying a grain which also contained planar defects. The percentage of grains for which mechanical twinning and epsilon martensite reflections were observed in <101> SAED patterns is also reported in Table 4 and indicates that an increased strain rate results in a modest increase in the fraction of grains with twins, but a slight decrease in the fraction of grains containing epsilon martensite. A slight decrease (265–211 nm) in the spacing between twins was observed for higher strain rates, as seen in Fig. 12. However, ECCI and DF-TEM distributions shown in Figs. 11 and 12 do not reveal significant trends in the effect of strain rate ( $\dot{\epsilon} = 2 \times 10^{-4}$  to  $\dot{\epsilon} = 2 \times 10^0$  /s) on the thickness and spacing of planar defects in samples interrupted at  $\epsilon_{\text{eng.}} = 0.18$  and 0.17 engineering strain.



**Fig. 9.** In a sample interrupted at  $\epsilon_{\text{eng.}} = 0.2$  at  $\dot{\epsilon} = 2 \times 10^2$  /s with the 0.95 mm sheet, a) non-matrix diffraction spots in the [110] gamma SAED pattern, (epsilon martensite is “ $\epsilon$ ”, deformation twinning is “ $T$ ” and  $dd_\epsilon$  is double diffraction contributed from the  $\{0-11-1\}$  and  $\{01-10\}$  hexagonal epsilon martensite reflections [4]). A centered objective aperture was used to form b) respective dark field images and the bright field image for continuity. Diffraction analysis indicates  $\epsilon$ -martensite platelets (left/blue) and deformation twinning (right/red) are observed after interruption at high strain rates.

## 4. Discussion

### 4.1. Techniques for measuring high strain rate tensile properties

As strain rate is increased from quasi-static strain rates ( $\dot{\epsilon} = 10^{-5}$  /s to  $\dot{\epsilon} = 10^0$  /s) to dynamic-low strain rates ( $\dot{\epsilon} = 10^0$  /s to  $\dot{\epsilon} = 10^3$  /s), dynamic considerations of the mechanical resonance in the test specimen and tensile testing machine become more important [41]. Consistent with Meyers’ [41] recommendations on common testing methods, the International Iron and Steel Institute [57] also recommends the use of servo-hydraulics to evaluate mechanical properties of sheet steels, within the strain rate range of  $\dot{\epsilon} = 10^{-1}$  /s to  $\dot{\epsilon} = 10^2$  /s. Below  $\dot{\epsilon} = 10^3$  /s, oscillations in the load data are purely due to mechanical resonance in the testing setup, for materials which do not exhibit dynamic strain aging effects. Inertial effects of plastic-wave, shear-wave and shock-wave propagation are only considered at strain rates of  $\dot{\epsilon} = 10^3$  /s and greater [41]. As detailed in Section 2.4, the load ringing amplitude can be minimized by reducing the mass between the gage section and the load measuring device [41,42] or using two elastic strain gages on each side of the grip section [43]. Avoiding the use of extensometers for strain measurement and implementing load oscillation reduction procedures are necessary steps to evaluate the dynamic tensile properties of next generation advanced high strength steels [57].

The present work uses titanium grips to reduce mass (between the tensile specimen and load washer) and strain gages to minimize non-linearity in strain measurement, the limitations of which are outlined in Section 2.4. Supplementary Fig. S4 compares the use of two different methods to minimize ringing in stress-strain measurements, but the techniques are not foolproof. Rather, the software-based method implemented in this work likely underestimates the yield strength and initial strain-hardening rates during tests at  $\dot{\epsilon} = 2 \times 10^2$  /s. Large amplitudes of load ringing during tests at  $\dot{\epsilon} = 2 \times 10^2$  /s and the maximum frame rate of the thermal camera (5 ms per frame) significantly reduces the ability to accurately measure stress, strain and adiabatic heating. Simply put, mechanical resonance at high strain rates inherently affects data quality, specifically in the initial values of strain when the oscillation amplitude from the actuator’s engagement with the test specimen is greatest [57]. Therefore, interpretation of any changes in tensile behavior or strain-hardening rate during initial values of strain should be carefully considered during high strain rate tests.

### 4.2. Influence of strain rate and adiabatic heating on deformation mechanisms

High strain rate testing does not allow sufficient time for heat to

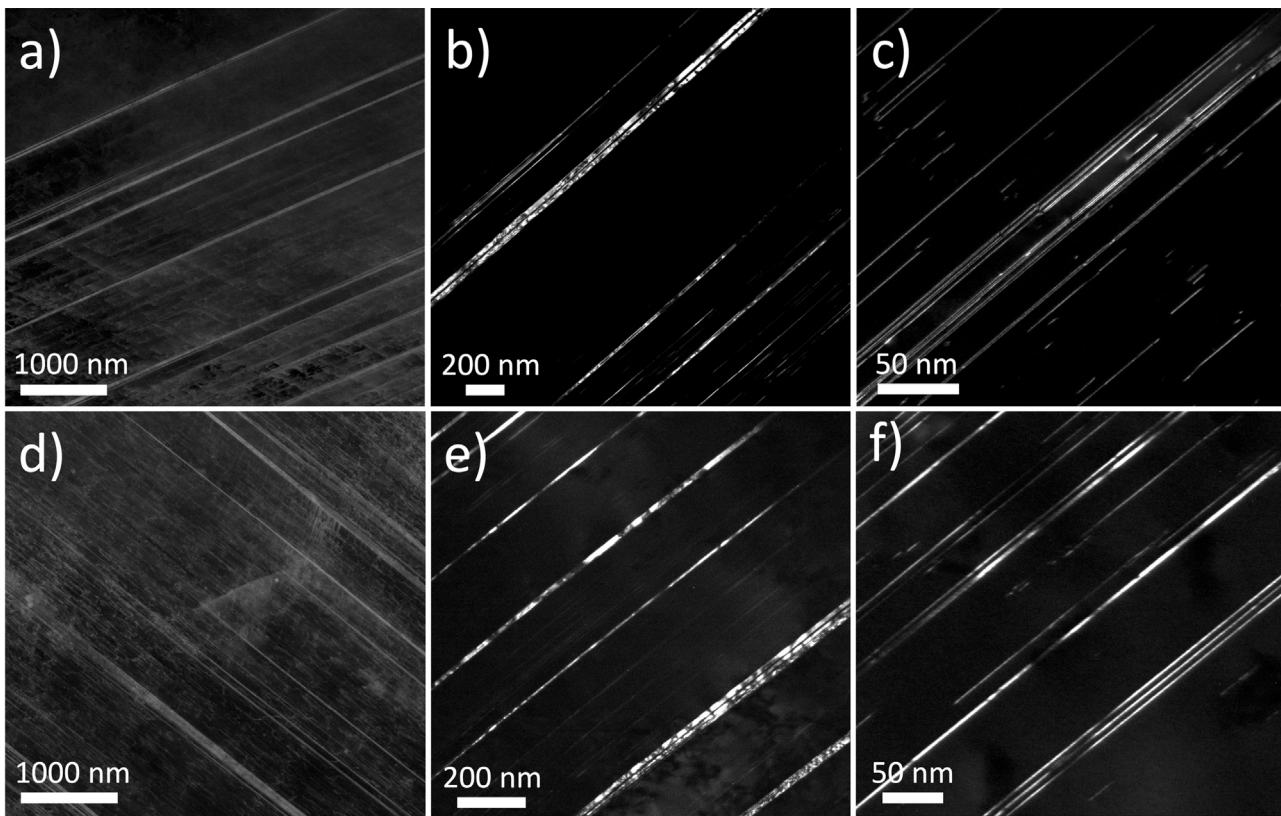


**Fig. 10.** Representative images of planar defects characterized in specimens of the same sheet thickness (1.15 mm) tested at (a–c)  $\dot{\epsilon} = 2 \times 10^0$  /s and interrupted at  $\epsilon_{\text{eng.}} = 0.18$  and (d–f) tested at  $\dot{\epsilon} = 2 \times 10^{-4}$  /s and interrupted at  $\epsilon_{\text{eng.}} = 0.17$ . Characterization techniques shown are (a, d) ECI, (b, e) twin reflections selected to form a DF-TEM image and (c, f) epsilon martensite reflections selected to form a DF-TEM image. Twin and martensite reflections were selected from the same SAED pattern and thus the same grain of interest. The differentiation of twinning from epsilon martensite by DF-TEM is also described in detail in the caption of Fig. 9.

diffuse from the interior of a tensile specimen to the free surfaces and subsequently be lost to the environment, which leads to adiabatic heating [41]. As specimen thickness increases, adiabatic heating may also occur at even lower strain rates [41,58]. The evolution of the temperature increase during deformation is important since different temperature-dependent deformation modes may be activated during a single test. Furthermore, the significant adiabatic heating that may occur at high strain rates, along with the effect of strain rate on the thermal component of flow stress, can lead to complicated mechanical behavior of TWIP steels [73].

In the current work, a high-speed thermal camera was used to measure the increase in specimen temperature as a function of time and thus strain for these tests. The rise in specimen temperature from room temperature (23 °C) to 83 °C (average temperature at maximum uniform elongation for all tests at  $\dot{\epsilon} = 2 \times 10^1$ ) was input into a thermodynamic model and predicts a rise in SFE from 21 to 35 mJ/m<sup>2</sup> for the Fe-25Mn-3Al-3Si (wt%) alloy. In previous work, the influence of SFE on the microstructural evolution and mechanical properties of a Fe-25Mn-3Al-3Si and a Fe-28Mn-3Al-3Si alloy were evaluated during RT tensile deformation at quasi-static strain rates (where adiabatic heating was insignificant) [4]. The measured RT SFE of the Fe-25Mn-3Al-3Si and Fe-28Mn-3Al-3Si alloys are 21 and 39 mJ/m<sup>2</sup>, respectively [14]. The Fe-25Mn-3Al-3Si alloy exhibited both planar and wavy deformation characteristics along with the formation of both mechanical twins and epsilon martensite. In contrast, the Fe-28Mn-3Al-3Si alloy exhibited a greater propensity for cross slip, a more wavy dislocation structure, and mechanical twinning was the dominant secondary deformation mechanism with no significant observations of epsilon martensite formation. It is also notable that in that work, increasing the SFE from 21 to 39 mJ/m<sup>2</sup> by increasing Mn content only slightly reduced strength and ductility during RT deformation [4]. In summary, the

largest predicted rise in SFE from adiabatic heating at high strain rates in the present work is expected to have only a small effect on UTS and UE, based on studies of similar Fe-Mn-Al-Si steels with different SFE values.

The combined effects of strain rate on dislocation slip and continued refinement of the dislocation substructure by planar defects, (referred to as the dynamic Hall-Petch effect), are important considerations in this work when considering differences in substructure spacing and dislocation mean free paths [26,59]. Micro-hardness measurements were completed on samples interrupted and pulled-to-failure at all strain rates in the present work, but did not show any statistically significant difference in micro-hardness at any given strain rate for the same nominal strain. Rather, the micro-hardness measurements only showed a statistically significant increase in hardness with increasing engineering strain. These results may indicate that the microstructure evolution at different strain rates is similar or that any microstructural differences that exist do not significantly influence the hardness.

Although deformation twinning has been previously confirmed with DF-TEM, hexagonal epsilon martensite was not observed as a deformation mechanism in the Fe-25Mn-3Al-3Si alloy (using XRD and DF-TEM) by Grässel et al., regardless of strain rate. However, recent work by Pierce et al. [14], which was conducted at quasi-static strain rates, identified epsilon martensite with DF-TEM. The present work reports the first observation of both deformation twinning and hexagonal epsilon martensite in the same grain taken from samples of the Fe-25Mn-3Al-3Si alloy deformed at high strain rates. These results are a strong indicator that the microstructure is similar at quasi-static and high strain rates. As has been reported previously, the critical resolved shear stress required for a leading partial dislocation to break away from the trailing dislocation is more sensitive to temperature and SFE than strain rate in the context of producing a large effect on the twin volume



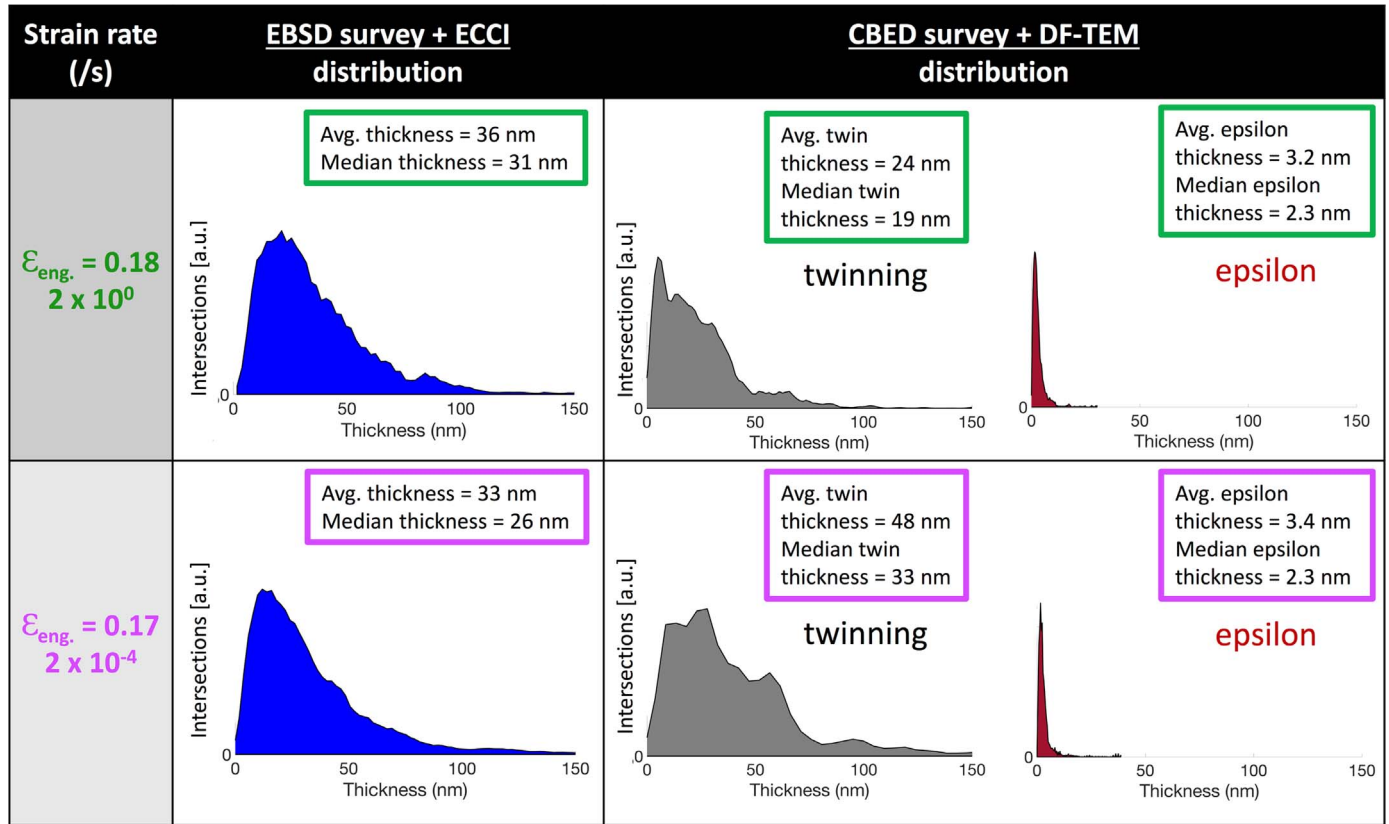


Fig. 11. Quantitative thickness measurements from SEM & TEM techniques based on tensile specimens from the same sheet thickness (1.15 mm), interrupted at  $\epsilon_{eng.} = 0.18$  tested at  $\dot{\epsilon} = 2 \times 10^0$  /s and  $\epsilon_{eng.} = 0.17$  tested at  $\dot{\epsilon} = 2 \times 10^{-4}$  /s.

fraction [15,19]. More importantly the sensitivity of the flow stress to thermally-activated short-range barriers indicates that any change in the volume fraction or onset of mechanical twinning caused by high strain rates may not be the main contributor to observable changes in work-hardening. The sensitivity of the strain-hardening behavior may suggest the main contributing factor to the increased flow stress in the current work at relatively high strain rates is related to the dislocation mean free path [19,34] and an increase in flow stress for dislocation glide to overcome short-range barriers with increasing strain rate. This explanation is more likely than a significant change in the dynamics of mechanical twinning or epsilon martensite formation within the studied range of strain rates, as both planar defects are still observed at low and high strain rates for this alloy. The strain-hardening rate for the tests at  $\dot{\epsilon} = 2 \times 10^{-2}$  /s possess the lowest value at initial stages of

accumulated strain as compared to all other strain rates, which is consistent with observations by Grässel et al. [8]. Lee et al. reported a minimum strain-hardening rate for a strain rate of  $\dot{\epsilon} = 10^{-3}$  /s at which the critical resolved shear stress (CRSS) of the strain-induced martensite and dislocation slip was lower [and favored] as compared to twinning [20]. In the present study, the real reason for the low values of strain-hardening rate of the  $\dot{\epsilon} = 2 \times 10^{-2}$  /s as compared to those at higher strain rates is likely quite complex and most likely dependent on multiple mechanisms related to dislocation mobility and planar defect generation.

Christian and Mahajan have stated that an increase in strain-rate generally leads to an increase in twinning activity [60]. Other researchers have observed twinning after shock loading in FCC materials that do not twin under quasi-static deformation conditions, such as

Table 4

Comparison of SEM and TEM-based techniques used to survey grains in samples interrupted to nominally the same level of engineering strain at different strain rates ( $\dot{\epsilon} = 2 \times 10^{-4}$  /s and  $\dot{\epsilon} = 2 \times 10^0$  /s). Both tensile specimens were machined from the same 1.15 mm thick sheet. \*some grains contained both twins and hexagonal epsilon martensite platelets.

Engineering strain and strain rate (/s)	Characterization techniques to measure # of grains with planar defects	
	Bulk samples: EBSD + ECCI	Thin foil samples: DF-TEM
$\epsilon_{eng.} = 0.18$ at $\dot{\epsilon} = 2 \times 10^0$ /s	51% of 37 surveyed grains, (with $\langle 110 \rangle$ orientation and optimal channeling conditions), contained planar defects	52% of 23 surveyed grains contained planar defects* 52% of 23 surveyed grains contained twinning 17% of 23 surveyed grains contained epsilon martensite
$\epsilon_{eng.} = 0.17$ at $\dot{\epsilon} = 2 \times 10^{-4}$ /s	47% of 34 surveyed grains, (with $\langle 110 \rangle$ orientation and optimal channeling conditions), contained planar defects	42% of 24 surveyed grains contained planar defects* 38% of 24 surveyed grains contained twinning 33% of 24 surveyed grains contained epsilon martensite

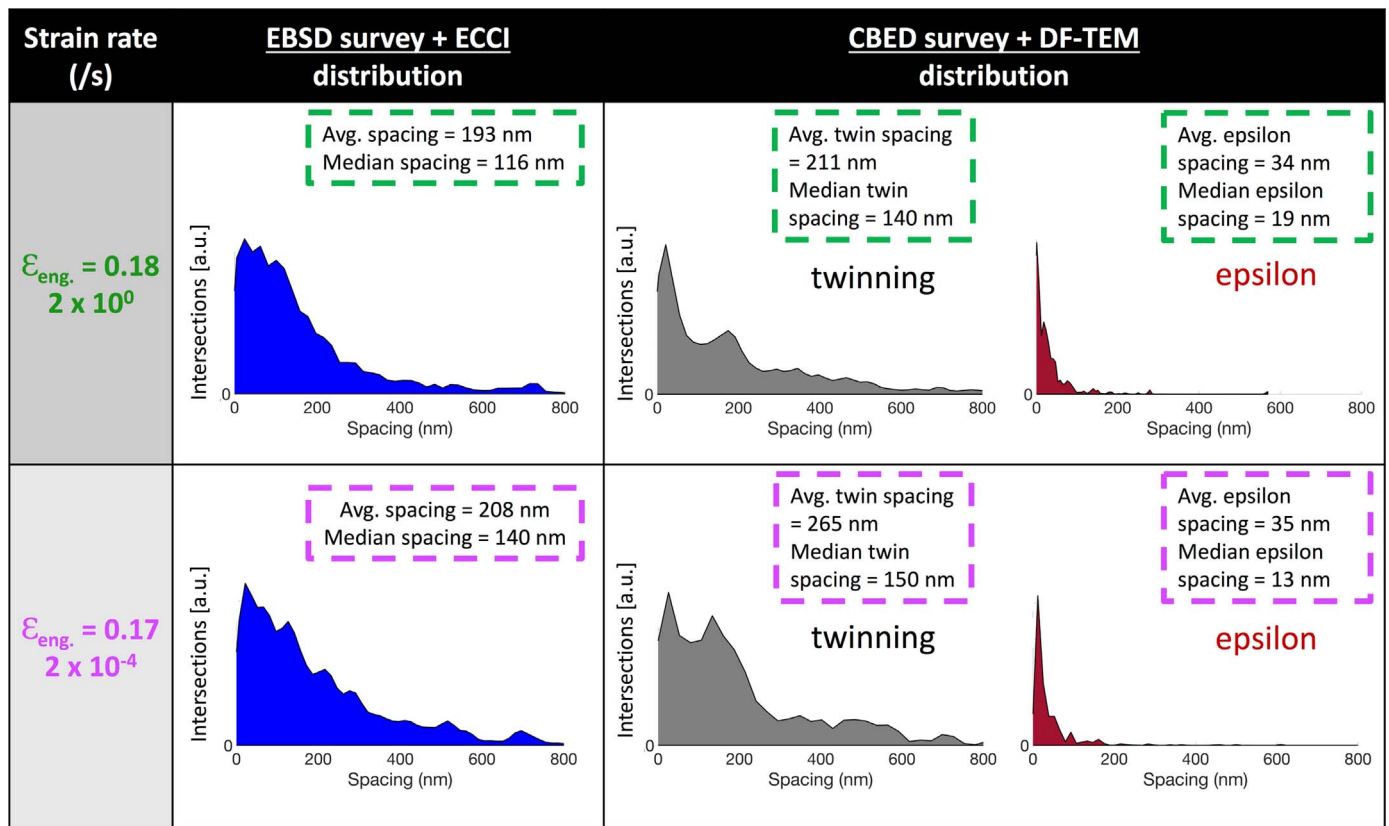


Fig. 12. Quantitative spacing measurements from SEM & TEM techniques based on tensile specimens from the same sheet thickness (1.15 mm), interrupted at  $\epsilon_{\text{eng.}} = 0.18$  tested at  $\dot{\epsilon} = 2 \times 10^0$  /s and  $\epsilon_{\text{eng.}} = 0.17$  tested at  $\dot{\epsilon} = 2 \times 10^{-4}$  /s.

aluminum alloys [60]. In another study, microstructural evaluation of an Fe-18Mn-1.22Al-0.56C alloy showed adiabatic shear banding and twinning after ballistic testing at  $\dot{\epsilon} = 10^5$  /s [61]. As Steinmetz et al. [23] pointed out, quantifying twin volume fractions is difficult due to the heterogeneous nature of grains and the observation that twins may not completely cross the full diameter in each grain. Therefore, in the present work careful image processing techniques were used to quantify all observable features in a given field of view for each imaging technique. The drawbacks of comparing ECCI and DF-TEM techniques are evident due to the point-to-point resolution limit of ECCI techniques ( $\sim 8$ – $10$  nm) [49], the characterization of only one variant of planar defects in the SAED pattern for a given grain and the limited number of observable grains in electro-polished TEM samples. Further, the slight decrease in frequency of observed martensite reflections in SAED patterns at higher strain rates (see Table 4) could either be due to the rise in SFE [14,21,62], (in this case from adiabatic heating) or simply because the hexagonal platelets are too thin to contribute to the SAED pattern [56]. A slight decrease in twin spacing with increased strain rate is observed and is consistent with observations of an increase in twin volume fraction by other TWIP steel researchers [8,11,54]. In contrast, Steinmetz et al. also pointed out that an increase in twinning volume fraction at higher strain rates was observed in simulation and experiment, but the contribution to strain-hardening was not significant [23]. An important observation in the current work is that TWIP and TRIP effects are observed by DF-TEM at all strain rates for the Fe-25Mn-3Al-3Si alloy, (which has a room temperature SFE of  $21 \text{ mJ/m}^2$ ). Thus, there is most likely not a significant change in the dominant mechanism within the range of strain rates investigated (from  $\dot{\epsilon} = 10^{-4}$  /s to  $\dot{\epsilon} = 10^2$  /s).

#### 4.3. Effects of strain rate and specimen thickness on tensile properties

High strain rate deformation reduces the time for dislocations to

overcome short-range dislocation barriers, which causes an increase in flow stress [10]. Allain et al. reported that the short-range barriers in austenitic steels responsible for the thermal and strain rate dependence of the yield strength are the sum of contributions from solid solution and thermally-activated contributions from a viscoplastic potential [64,65]. Similar to the present work on Fe-25Mn-3Al-3Si (wt%), there is a notable strain rate sensitivity of the yield strength. Surprisingly, Allain et al. reported that large amounts of Mn [20–30 wt%] and Al [0–3 wt%] contents do not play significant roles on the activation volume of thermally-dependent barriers to dislocation mobility. However, Allain et al. specifically noted that approximately 3 wt% Si has a remarkable effect on dislocation mobility by significantly reducing the apparent activation volume and mean free path. The activation volume of thermally-dependent short-range barriers and dislocation mean free path respectively influence the yield strength and work-hardening. Previous research on Si-containing TWIP steels revealed a distinct sensitivity in yield strength and work-hardening at strain rates lower than predicted as compared to Fe-Mn-C alloys (steel systems not containing silicon) [8,64]. In summary, the increase in flow stress necessary for partial dislocations to overcome thermally-dependent short-range barriers during dislocation glide with increasing strain rate explains the positive strain rate sensitivity of the yield strength in the present work on the Fe-25Mn-3Al-3Si (wt%) steel and is consistent with previous work [29,64,66].

A previous study on a Fe-25Mn-3Al-3Si (wt%) steel by Grässel et al. [8] shows similar trends in mechanical properties as a function of strain rate, as compared to the present study on a steel alloy with the same nominal composition. Specifically, the trends show that with increasing strain rate, YS increases significantly, UTS increases modestly and UE decreases modestly, as seen in Fig. 5. Curtze and Kuokkala's work [10] on a high-Mn TWIP steel also showed a positive strain rate sensitivity for YS and UTS within the same range of strain rates. Lichtenfeld et al. [67] also found increases in YS and UTS and a decrease in UE with

increasing strain rate for type 309 stainless steel consisting of stable austenite. In the present work, an increase in strain rate also increased the PSE, which is consistent with other TWIP steel research [8,20,63,66,68–70]. Furthermore, PSE values at strain rates of  $\dot{\epsilon} = 2 \times 10^{-2}$  and  $\dot{\epsilon} = 2 \times 10^2$  /s are greater for the 1.15 mm sheet thickness than for the 0.95 mm sheet thickness in the present work. Previous research corroborates the present work in that the yield strength and uniform elongation are independent of sheet thickness [29,30,32,33,71,72]. Post-uniform elongation depends on the stress distribution of the necked region, which itself is dependent on specimen thickness for specimens with rectangular cross sections [32]. More specifically, Yuan et al. reported that increasing the thickness of specimens with rectangular cross sections resulted in longer regions of the neck being exposed to stress levels greater than the yield point of the material (X80 steel), ultimately resulting in more diffuse necking and greater post uniform elongation [32]. These observations are consistent with current work as post-uniform elongation is greater for the 1.15 mm thick sheet as compared to the 0.95 mm sheet for samples deformed at the same strain rate ( $\dot{\epsilon} = 2 \times 10^{-2}$  and  $\dot{\epsilon} = 2 \times 10^2$  /s).

As seen in Fig. 5, the YS and UTS strain rate sensitivities are very similar between  $\dot{\epsilon} = 2 \times 10^{-2}$  and  $\dot{\epsilon} = 2 \times 10^2$  /s, whereas the UTS strain rate sensitivity is lower than the YS strain rate sensitivity from  $\dot{\epsilon} = 2 \times 10^{-4}$  to  $\dot{\epsilon} = 2 \times 10^{-2}$  /s. Mechanical twins and epsilon martensite laths develop before  $\epsilon_{\text{eng.}} = 0.1$ . The planar defects act as obstacles to partial dislocation motion during slip on other glide planes, which increases the work-hardening capacity by reducing the mean free path of dislocations and leads to a higher UTS [4]. As strain increases, the dislocation density increases and eventually planar defects develop, which are barriers to dislocation motion on non-coplanar slip systems [21,32]. As no significant differences in micro-hardness were measured with an increase in strain rate for the same nominal strain and both twins and epsilon martensite are observed at the lowest and highest strain rate, the cause of increase in ultimate tensile strength with increasing strain rate is most likely due to a modest decrease of spacing between twins, an increase in forest dislocation density or simply because the reduced time for dislocations to overcome short-range dislocation barriers causes an increase in flow stress [10].

However, as strain rate increases, UE decreases and TE increases, indicating an increased likelihood of strain localizations at lower strains at higher strain rates [74]. Early work on the Fe-25Mn-3Al-3Si alloy by Frommeyer [8,75] also measured a decrease in UE with an increase in strain rate, which was attributed to specimen softening from adiabatic heating, but the heating was not experimentally measured. Further, a significant decrease in YS, UTS, UE and TE with increasing environment testing temperature has been observed in work on alloys of nominally the same composition [8,36]. With increasing strain rate from  $\dot{\epsilon} = 2 \times 10^{-2}$  /s to  $\dot{\epsilon} = 2 \times 10^2$  /s, reduction in area remains approximately constant but post-uniform elongation increases. In the present work, these mechanical test results, in combination with thermal imaging that revealed multiple localized regions of greater temperature at strain rates of  $\dot{\epsilon} = 2 \times 10^1$  /s and  $\dot{\epsilon} = 2 \times 10^2$  /s (see Fig. 5 and S8), suggest that multiple areas of strain localization are occurring at the higher strain rates and are contributing to the post uniform elongation. The wider difference in temperature for tests at the same strain rate as well as the observation of localized heating, which corresponds to strain localizations [23], is consistent with observations by other TWIP steel researchers [74,76]. Grässel et al. also observed a large difference in TE and UE (increased post-uniform elongation) at strain rates above  $\dot{\epsilon} = 10^{-1}$  /s for the Fe-25Mn-3Al-3Si alloy [8]. Moreover, multiple strain localizations at larger levels of strain and increased adiabatic heating is likely the cause of a decrease in uniform elongation with respect to an increase in strain rate.

## 5. Conclusions

- The 0.2% offset yield strength of the Fe-25Mn-3Al-3Si (wt%) alloy

increased by approximately 64% in the strain rate range of  $\dot{\epsilon} = 2 \times 10^{-4}$  to  $\dot{\epsilon} = 2 \times 10^2$  /s. The positive yield strength strain rate sensitivity is likely due to an increase in flow stress necessary for partial dislocations to overcome thermally-dependent short-range barriers during dislocation glide with increasing strain rate.

- The product of [ultimate tensile] strength and [total] elongation (PSE) increases with increasing strain rate and sheet thickness. Sheet thickness did not affect the magnitude of the yield strength, yield strength strain rate sensitivity, or uniform elongation.
- Increasing strain rate from  $\dot{\epsilon} = 2 \times 10^{-2}$  /s to  $\dot{\epsilon} = 2 \times 10^2$  /s increased the amount of post-uniform elongation. As reduction-in-area measurements on the necked regions did not change significantly for this range of strain rates, strain localization is the likely mechanism, which is supported by localized regions of higher temperatures observed in thermal imaging during tests at  $\dot{\epsilon} = 2 \times 10^1$  and  $\dot{\epsilon} = 2 \times 10^2$  /s.
- The average tensile specimen temperature increased with increasing strain and strain rate at rates from  $\dot{\epsilon} = 10^{-2}$  /s to  $\dot{\epsilon} = 10^2$  /s. The thermodynamic model used to correlate specimen temperature with SFE predicts an increase from 21 mJ/m<sup>2</sup> at room temperature (23 °C) to ~ 34 mJ/m<sup>2</sup> at 83 °C. An increase in SFE of this magnitude is expected to have only a small effect on tensile properties.
- Deformation twinning and epsilon martensite are observed in tensile specimens interrupted from quasi-static ( $\dot{\epsilon} = 2 \times 10^{-4}$  /s) through low-dynamic ( $\dot{\epsilon} = 2 \times 10^2$  /s) strain rates. ECCI and DF-TEM measurements do not reveal a statistically significant effect of strain rate on the thickness and spacing of mechanical twins or epsilon martensite laths in the Fe-25Mn-3Al-3Si (wt%) steel.

## Acknowledgements

This work was funded by the US National Science Foundation, Division of Materials Research under grant DMR1309258, NSF EPS 1004083, the Advanced Steel Processing and Products Research Center at Colorado School of Mines and the Max Planck Institut für Eisenforschung in Düsseldorf, Germany. We are grateful for guidance from Angelika Bobrowski and Katja Angenendt (MPIE) with TEM and SEM sample preparation, respectively. Prof D.G. Walker (Vanderbilt University) generously provided the infra-red camera.

## Appendix A. Supporting information

Supplementary data associated with this article can be found in the online version at <http://dx.doi.org/10.1016/j.msea.2017.11.017>.

## References

- [1] J. Dykeman, Advanced high strength steel – recent progress, ongoing challenges, and future opportunities, in: Proceedings of the International Symposium on New Developments in Advanced High-Strength Sheet Steels, 2013, pp. 15–28.
- [2] P.J. Belanger, P.J. Hall, J.J. Coryell, J.P. Singh, Automotive body press-hardened steel Trends, in: Proceedings of the International Symposium on New Developments in Advanced High-Strength Sheet Steels, 2013, pp. 239–250.
- [3] Advanced High Strength Steel (AHSS) Application Guidelines, International Iron & Steel Institute, Committee on Automotive Applications. [Online], 2009. Available: <[www.worldautosteel.org](http://www.worldautosteel.org)>.
- [4] D.T. Pierce, J.A. Jiménez, J. Bentley, D. Raabe, J.E. Wittig, The influence of stacking fault energy on the microstructural and strain-hardening evolution of Fe-Mn-Al-Si steels during tensile deformation, *Acta Mater.* 100 (2015) 178–190.
- [5] O. Bouaziz, S. Allain, C.P. Scott, P. Cugy, D. Barbier, High manganese austenitic twinning induced plasticity steels: a review of the microstructure properties relationships, *Curr. Opin. Solid State Mater. Sci.* 15 (4) (2011) 141–168.
- [6] K. Jeong, J.E. Jin, Y.S. Jung, S. Kang, Y.K. Lee, The effects of Si on the mechanical twinning and strain hardening of Fe-18Mn-0.6C twinning-induced plasticity steel, *Acta Mater.* 61 (9) (2013) 3399–3410.
- [7] S. Allain, J.P. Chateau, O. Bouaziz, S. Migot, N. Guelton, Correlations between the calculated stacking fault energy and the plasticity mechanisms in Fe-Mn-C alloys, *Mater. Sci. Eng. A* 387–389 (1–2) (2004) 158–162 (SPEC. ISS).
- [8] O. Grässel, L. Krüger, G. Frommeyer, L.W. Meyer, High strength Fe-Mn-(Al, Si) TRIP/TWIP steels development - properties – application, *Int. J. Plast.* 16 (10) (2000) 1391–1409.
- [9] J. Kim, S.J. Lee, B.C. De Cooman, Effect of Al on the stacking fault energy of Fe-



- 18Mn-0.6C twinning-induced plasticity, *Scr. Mater.* 65 (4) (2011) 363–366.
- [10] S. Curtze, V.T. Kuokkala, Dependence of tensile deformation behavior of TWIP steels on stacking fault energy, temperature and strain rate, *Acta Mater.* 58 (15) (2010) 5129–5141.
- [11] D. Raabe, et al., Ab initio-guided design of twinning-induced plasticity steels, *MRS Bull.* 41 (4) (2016) 320–325.
- [12] S. Lee, B.C. De Cooman, Annealing temperature dependence of the tensile behavior of 10 pct Mn multi-phase TWIP-TRIP steel, *Metall. Mater. Trans. A Phys. Metall. Mater. Sci.* 45 (13) (2014) 6039–6052.
- [13] I. Gutierrez-Urrutia, D. Raabe, Multistage strain hardening through dislocation substructure and twinning in a high strength and ductile weight-reduced Fe-Mn-Al-C steel, *Acta Mater.* 60 (16) (2012) 5791–5802.
- [14] D.T. Pierce, J.A. Jimenez, J. Bentley, D. Raabe, C. Oskay, J.E. Wittig, The influence of manganese content on the stacking fault and austenite/epsilon-martensite interfacial energies in Fe-Mn-(Al-Si) steels investigated by experiment and theory, *Acta Mater.* 68 (2014) 238–253.
- [15] O. Grässel, G. Frommeyer, C. Derder, H. Hofmann, Phase transformations and mechanical properties of Fe-Mn-Si-Al TRIP-Steels, *Le. J. Phys. IV* 7 (C5) (1997) 383–388.
- [16] A. Dumay, J.P. Chateau, S. Allain, S. Migot, O. Bouaziz, Influence of addition elements on the stacking-fault energy and mechanical properties of an austenitic Fe-Mn-C steel, *Mater. Sci. Eng. A* 483–484 (1–2C) (2008) 184–187.
- [17] A. Saeed-Akbari, J. Imlau, U. Prah, W. Bleck, Derivation and variation in composition-dependent stacking fault energy maps based on subregular solution model in high-manganese steels, *Metall. Mater. Trans. A Phys. Metall. Mater. Sci.* 40 (13) (2009) 3076–3090.
- [18] M. Pozuelo, J.E. Wittig, J.A. Jiménez, G. Frommeyer, Enhanced mechanical properties of a novel high-nitrogen Cr-Mn-Ni-Si austenitic stainless steel via TWIP/TRIP effects, *Metall. Mater. Trans. A Phys. Metall. Mater. Sci.* 40 (8) (2009) 1826–1834.
- [19] S. Kibey, J.B. Liu, D.D. Johnson, H. Sehitoglu, Predicting twinning stress in fcc metals: linking twin-energy pathways to twin nucleation, *Acta Mater.* 55 (20) (2007) 6843–6851.
- [20] S. Lee, Y. Estrin, B.C. De Cooman, Effect of the strain rate on the TRIP-TWIP transition in austenitic Fe-12 pct Mn-0.6 pct C TWIP Steel, *Metall. Mater. Trans. A Phys. Metall. Mater. Sci.* 45 (2) (2014) 717–730.
- [21] A. Saeed-Akbari, L. Mosecker, A. Schwedt, W. Bleck, Characterization and prediction of flow behavior in high-manganese twinning induced plasticity steels: Part I. mechanism maps and work-hardening behavior, *Metall. Mater. Trans. A* 43 (5) (2012) 1688–1704.
- [22] S.L. Wong, M. Madivala, U. Prah, F. Roters, D. Raabe, A crystal plasticity model for twinning- and transformation-induced plasticity, *Acta Mater.* 118 (2016) 140–151.
- [23] D.R. Steinmetz, et al., Revealing the strain-hardening behavior of twinning-induced plasticity steels: theory, simulations, experiments, *Acta Mater.* 61 (2) (2013) 494–510.
- [24] O. Bouaziz, S. Allain, C.P. Scott, P. Cugy, D. Barbier, High manganese austenitic twinning induced plasticity steels: a review of the microstructure properties relationships, *Curr. Opin. Solid State Mater. Sci.* 15 (2011) 141–168.
- [25] B.C. De Cooman, Y. Estrin, S.K. Kim, Twinning-induced plasticity (TWIP) steels, *Acta Mater.* (2017) 1–80.
- [26] I. Gutierrez-Urrutia, D. Raabe, Dislocation and twin substructure evolution during strain hardening of an Fe-22 wt% Mn-0.6 wt% C TWIP steel observed by electron channeling contrast imaging, *Acta Mater.* 59 (16) (2011) 6449–6462.
- [27] M. Seth, V.J. Vohnout, G.S. Daehn, Formability of steel sheet in high velocity impact, *J. Mater. Process. Technol.* 168 (3) (2005) 390–400.
- [28] S. Hiermaier, *Structures under crash and impact: continuum mechanics, discretization and experimental characterization*, New York, 2008.
- [29] B. Strudel, J. Brumek, Effect of tensile test specimen size on ductility of R7T steel, *Metall. Mater. Sci. Eng. A* 532 (2013) 2–7.
- [30] D.R. Malpally, *Uncertainty Analysis of Mechanical Properties From Miniature Tensile Testing of High Strength Steels*, Utah State University, 2014.
- [31] X. Sun, A. Soulam, K.S. Choi, O. Guzman, W. Chen, Effects of sample geometry and loading rate on tensile ductility of TRIP800 steel, *Mater. Sci. Eng. A* 541 (2012) 1–7.
- [32] W.J. Yuan, Z.L. Zhang, Y.J. Su, L.J. Qiao, W.Y. Chu, Influence of specimen thickness with rectangular cross-section on the tensile properties of structural steels, *Mater. Sci. Eng. A* 532 (2012) 601–605.
- [33] K. Wang, D. Wang, F. Han, Effect of sample thickness on the tensile behaviors of Fe-30Mn-3Si-3Al twinning-induced plasticity steel, *Mater. Sci. Eng. A* 642 (2015) 249–252.
- [34] I.F. Rajendran, Inertia effects on the ductile failure of thin rings, *J. Appl. Mech.* 49 (1982) 31–36.
- [35] I. Choi, S. Lee, D.K. Matlock, J.G. Speer, Strain control during high speed tensile testing, *J. Test. Eval.* 34 (5) (2006) 5–8.
- [36] D.T. Pierce, The Influence of Manganese Content and Temperature on the Relative FCC/HCP Phase Stability and Strain-Hardening Behavior of High-Manganese TRIP/TWIP Steels, *Vanderbilt University*, 2014.
- [37] D.T. Pierce, J. Bentley, J.A. Jiménez, J.E. Wittig, Stacking fault energy measurements of Fe-Mn-Al-Si austenitic twinning-induced plasticity steels, *Scr. Mater.* 66 (10) (2012) 753–756.
- [38] D.T. Pierce, K. Nowag, A. Montagne, J.A. Jiménez, J.E. Wittig, R. Ghisleni, Single crystal elastic constants of high-manganese transformation- and twinning-induced plasticity steels determined by a new method utilizing nanoindentation, *Mater. Sci. Eng. A* 578 (2013) 134–139.
- [39] E112-10.pdf, in *ASTM Designation E112-10*, West Conshohocken, PA: ASTM International, 2011.
- [40] L. Addessio, The Effect of Strain Rate and Tempering on the Mechanical Properties of Low Carbon Martensite, *Colorado School of Mines*, 2007.
- [41] M.A. Meyers, *Dynamic Behavior of Materials*, 1994.
- [42] D. Bruce, *Dynamic Tensile Testing of Sheet Steels and Influence of Strain Rate on Strengthening Mechanisms in Sheet Steels*, Colorado School of Mines, 2003.
- [43] X. Yang, L.G. Hector, J. Wang, A combined theoretical / experimental approach for reducing ringing artifacts in low dynamic testing with servo-hydraulic load frames, *Exp. Mech.* 54 (2014) 775–789.
- [44] D.B. Williams, C.Barry. Carter, *Transmission Electron Microscopy*, 2009.
- [45] D.R. Steinmetz, S. Zaefferer, Towards ultrahigh resolution EBSD by low accelerating voltage, *Mater. Sci. Technol.* 26 (6) (2010) 640–645.
- [46] I. Gutierrez-Urrutia, S. Zaefferer, D. Raabe, Coupling of electron channeling with EBSD: toward the quantitative characterization of deformation structures in the sem, *JOM* 65 (9) (2013) 1229–1236.
- [47] S. Zaefferer, On the formation mechanisms, spatial resolution and intensity of backscatter Kikuchi patterns, *Ultramicroscopy* 107 (2–3) (2007) 254–266.
- [48] I. Gutierrez-Urrutia, S. Zaefferer, D. Raabe, Electron channeling contrast imaging of twins and dislocations in twinning-induced plasticity steels under controlled diffraction conditions in a scanning electron microscope, *Scr. Mater.* 61 (7) (2009) 737–740.
- [49] S. Zaefferer, N.N. Elhami, Theory and application of electron channelling contrast imaging under controlled diffraction conditions, *Acta Mater.* 75 (154) (2014) 20–50.
- [50] J.M. Sosa, D.E. Huber, B. Welk, H.L. Fraser, *Integr. Mater. Manuf. Innov.* 3 (2014) 18.
- [51] D.K. Matlock, J.G. Speer, Third generation of AHSS: microstructure design concepts, *Microstruct. Texture Steels* (2009) 185–205.
- [52] D.K. Matlock, J.G. Speer, Design considerations for the next generation of advanced high strength sheet steels, in: *Proceedings of the 3rd International Conference on Adv. High Strength Steels*, 2006, pp. 1–8.
- [53] S. Curtze, V.T. Kuokkala, Dependence of tensile deformation behavior of TWIP steels on stacking fault energy, temperature and strain rate, *Acta Mater.* 58 (15) (2010) 5129–5141.
- [54] S.M. Cotes, A.F. Guillermet, M. Sade, Fcc/Hcp martensitic transformation in the Fe-Mn system: Part II. Driving force and thermodynamics of the nucleation process, *Metall. Mater. Trans. A* 35 (1) (2004) 83–91.
- [55] I.C. Jung, B.C. De Cooman, Temperature dependence of the flow stress of Fe-18Mn-0.6C-xAl twinning-induced plasticity steel, *Acta Mater.* 61 (18) (2013) 6724–6735.
- [56] J.W. Brooks, M.H. Loretto, R.E. Smallman, In situ observations of the formation of martensite in stainless steel, *Acta Metall.* 27 (12) (1979) 1829–1838.
- [57] M. Borsutzki, D. Cornette, Y. Kuriyama, A. Uenishi, B. Yan, E. Opbroek, Recommendations for dynamic tensile testing of sheet steels, *Intern. Iron Steel Inst.* (2005) August.
- [58] K.D. Clarke, *Influence of Strain Rate on the Mechanical Properties and Formability of Ferritic Stainless Steel*, Colorado School of Mines, 2002.
- [59] I. Gutierrez-Urrutia, D. Raabe, Grain size effect on strain hardening in twinning-induced plasticity steels, *Scr. Mater.* 66 (12) (2012) 992–996.
- [60] J.W. Christian, S. Mahajan, *Twinning*, *Prog. Mater. Sci.* 39 (1995) 1–157.
- [61] N. Li, et al., Localized amorphism after high-strain-rate deformation in TWIP steel, *Acta Mater.* 59 (16) (2011) 6369–6377.
- [62] A. Saeed-Akbari, A.K. Mishra, J. Mayer, W. Bleck, Characterization and prediction of flow behavior in high-manganese twinning induced plasticity steels: Part II. Jerky flow and instantaneous strain rate, *Metall. Mater. Trans. A Phys. Metall. Mater. Sci.* 43 (5) (2012) 1705–1723.
- [63] P. Sahu, S. Curtze, A. Das, B. Mahato, V.T. Kuokkala, S.G. Chowdhury, Stability of austenite and quasi-adiabatic heating during high-strain-rate deformation of twinning-induced plasticity steels, *Scr. Mater.* 62 (1) (2010) 5–8.
- [64] S. Allain, O. Bouaziz, J.P. Chateau, Thermally activated dislocation dynamics in austenitic FeMnC steels at low homologous temperature, *Scr. Mater.* 62 (7) (2010) 500–503.
- [65] C.M. Sellars, W.J. Tegard, *Mem. Sci. Rev. Met.* 63 (1966) 731.
- [66] G.T. (Rusty) Gray, High-strain-rate deformation: mechanical behavior and deformation substructures induced, *Annu. Rev. Mater. Res.* 42 (1) (2012) 285–303.
- [67] J.A. Lichtenfeld, M.C. Mataya, C.J. Van Tyne, Effect of strain rate on stress-strain behaviour of alloy 309 and 304L austenitic stainless steel, *Metall. Mater. Trans. A* 37 (January) (2006) 147–161.
- [68] Y. Ha, H. Kim, K.H. Kwon, S.G. Lee, S. Lee, N.J. Kim, Microstructural evolution in Fe-22Mn-0.4C twinning-induced plasticity steel during high strain rate deformation, *Metall. Mater. Trans. A Phys. Metall. Mater. Sci.* 46 (2) (2014) 545–548.
- [69] A. Khosravifard, Influence of high strain rates on the mechanical behavior of high manganese steels, *Iran. J. Mater. Form.* 1 (1) (2014) 1–10.
- [70] H.K. Yang, Y.Z. Tian, Z.J. Zhang, Z.F. Zhang, Different strain rate sensitivities between Fe-22Mn-0.6C and Fe-30Mn-3Si-3Al twinning-induced plasticity steels, *Mater. Sci. Eng. A* 655 (2016) 251–255.
- [71] L. Yang, L. Lu, The influence of sample thickness on the tensile properties of pure Cu with different grain sizes, *Scr. Mater.* 69 (3) (2013) 242–245.
- [72] Y.H. Zhao, et al., Influence of specimen dimensions on the tensile behavior of ultra-fine-grained Cu, *Scr. Mater.* 59 (6) (2008) 627–630.
- [73] U.F. Kocks, H. Mecking, Physics and phenomenology of strain hardening: the FCC case, *Prog. Mater. Sci.* 48 (3) (2003) 171–273.
- [74] Y.F. Shen, N. Jia, R.D.K. Misra, L. Zuo, Softening behavior by excessive twinning and adiabatic heating at high strain rate in a Fe-20Mn-0.6C TWIP steel, *Acta Mater.* 103 (2016) 229–242.
- [75] G. Frommeyer, U. Brück, P. Neumann, Supra-ductile and high-strength manganese-TRIP/TWIP steels for high energy absorption purposes, *ISIJ Int.* 43 (3) (2003) 438–446.
- [76] V. Tari, A.D. Rollett, H. El Kadiri, H. Beladi, A.L. Oppedal, R.L. King, The effect of deformation twinning on stress localization in a three dimensional TWIP steel microstructure, *Model. Simul. Mater. Sci. Eng.* 23 (4) (2015) 45010.